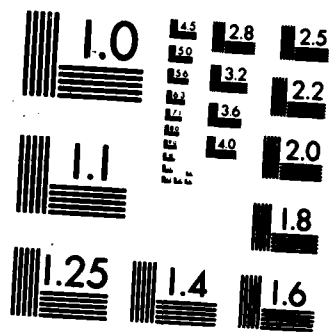


RESEARCH IN IMAGE UNDERSTANDING AS APPLIED TO 3-D
MICROWAVE TOMOGRAPHIC I. (U) MOORE SCHOOL OF ELECTRICAL
ENGINEERING PHILADELPHIA PA ELECTR. N H FARMAT
18 MAR 86 EO/MO-8 AFOSR-TR-86-0843 F/G 17/9

UNCLASSIFIED

F/G 17/9

NIL



MICROCOPY RESOLUTION TEST CHART
NATIONAL BUREAU OF STANDARDS-1963-A

AD-A173 063

2

UNIVERSITY OF PENNSYLVANIA
THE MOORE SCHOOL OF ELECTRICAL ENGINEERING
PHILADELPHIA, PA 19104

ANNUAL REPORT

RESEARCH IN IMAGE UNDERSTANDING AS APPLIED TO
3-D MICROWAVE TOMOGRAPHIC IMAGING WITH NEAR OPTICAL RESOLUTION

Prepared for

Air Force Office of Scientific Research
Building 410, Bolling Air Force Base
D.C. 20332

Under Grant
AFOSR 81-0240C

Prepared by
N.H. Farhat

Report Period
9/1/84 - 7/31/85

March 1986

~~EO/MO Report No. 8~~

DTIC
ELECTE
OCT 15 1986
S A D

DISTRIBUTION STATEMENT A
Approved for public release;
Distribution Unlimited

DTIC FILE COPY

86 10 10 058

UNCLASSIFIED

SECURITY CLASSIFICATION OF THIS PAGE (When Data Entered)

REPORT DOCUMENTATION PAGE		READ INSTRUCTIONS BEFORE COMPLETING FORM
1. REPORT NUMBER AFOSR-TR- 86-0843	2. GOVT ACCESSION NO. AD-A173013	3. RECIPIENT'S CATALOG NUMBER
4. TITLE (and Subtitle) RESEARCH IN IMAGE UNDERSTANDING AS APPLIED TO 3-D MICROWAVE TOMOGRAPHIC IMAGING WITH NEAR OPTICAL RESOLUTION		5. TYPE OF REPORT & PERIOD COVERED ANNUAL 9/1/84 - 7/31/85
7. AUTHOR(s) N.H. Farhat		6. PERFORMING ORG. REPORT NUMBER
9. PERFORMING ORGANIZATION NAME AND ADDRESS University of Pennsylvania 200 South 33rd Street Philadelphia, PA 19104		8. CONTRACT OR GRANT NUMBER(s) AFOSR 81-0240F
11. CONTROLLING OFFICE NAME AND ADDRESS Office of Research Administration 3451 Walnut Street Philadelphia, PA 19104		10. PROGRAM ELEMENT, PROJECT, TASK AREA & WORK UNIT NUMBERS 61102F 2305/B1
14. MONITORING AGENCY NAME & ADDRESS (if different from Controlling Office) United States Air Force Air Force Office of Scientific Research Building 410, Bolling AFB, DC 20332-6448		12. REPORT DATE March 10, 1986
		13. NUMBER OF PAGES
		15. SECURITY CLASS. (of this report) UNCLASSIFIED
		15a. DECLASSIFICATION/DOWNGRADING SCHEDULE
16. DISTRIBUTION STATEMENT (of this Report) Approved for public release; distribution unlimited.		
17. DISTRIBUTION STATEMENT (of the abstract entered in Block 20, if different from Report) Approved for public release; distribution unlimited.		
18. SUPPLEMENTARY NOTES		
19. KEY WORDS (Continue on reverse side if necessary and identify by block number) Microwave diversity imaging, reflection artefacts, polarization artefacts, imaging in severe clutter, neural net modeling, associative memory, sinogram classifier.		
20. ABSTRACT (Continue on reverse side if necessary and identify by block number) Our studies of the principles and methodologies of microwave diversity imaging employing angular (aspect dependent), spectral, and polarization diversities show that projection or tomographic images of radar targets can be achieved with near optical resolution. At this high resolution image artefact due to multiple reflections become important either as a degrading mechanism whose effect is to be minimized or as a mechanism for providing additional information about the object. For this reason a systematic study		

DD FORM 1 JAN 73 1473

EDITION OF 1 NOV 65 IS OBSOLETE

UNCLASSIFIED

SECURITY CLASSIFICATION OF THIS PAGE (When Data Entered)

UNCLASSIFIED

of multiple reflections between two simple bodies, two adjacent parallel conducting cylinders, was undertaken to determine the effect of multiple reflections on the image and the dependence on polarization of the incident field and the receiving antenna or antennas used to record the scattered field. Cylinders are chosen to make the problem analytically tractable and to provide analytical results against which experimentally obtained results can be compared. Excellent Agreement between experimental and analytical results was obtained. The results show that cross-polarized measurement, when the object is illuminated for example, by right-hand circularly polarized (RHCP) plane wave and the receiving antenna measuring the scattered field is left-hand circularly (LHCP), can be used to suppress the effect of multiple reflections between the cylinders and to eliminate noticeable artefact in the reconstructed image. This result can be readily interpreted by noting that reflections are specular and that the state of polarization is reversed after each specular reflection. If the receiver polarization on the other hand is RHCP, artefacts due to multiple scattering between the cylinders will appear in the image. The artefact does not correspond to any physical detail on the object, however, it can convey additional information about the imaging geometry. This study also illustrates well the power of microwave diversity imaging as a tool for the understanding of electromagnetic scattering.

A study of microwave diversity imaging in the presence of severe clutter as applicable to space-borne imaging of low flying objects and imaging of penetrable objects has also been undertaken. The results show that excellent image discrimination between the object and ground clutter can be realized provided that sufficiently wide spectral and angular windows are utilized.

We have also found that microwave diversity imaging furnishes images that have attributes that make them ideal for use in automated target recognition. These attributes include: (a) the image is always centered in the image plane, (b) the image is edge enhanced and hence resembles a "primal sketch" where detail, important for characterizing and recognizing the object is retained and all other detail, such as flat surfaces, is discarded reducing thereby the dimensionality of the signals being dealt with which is highly desirable for automated recognition, (c) although image information (Fourier space data) in microwave diversity imaging is obtained when looking at the object, for example from below, at a slant angle, the displayed image detail appears as if the object is observed directly from below. This is a consequence of the tomographic nature of microwave diversity imaging. All of the above features make the image information obtained ideal for the generation of target classifiers that are suitable for use in automated recognition schemes that might utilize associative memories based on models of neural networks. For this reason we have initiated a study of optical implementations of neural net models, where robustness and fault tolerant features of associative recall in these networks are combined with the parallelism and massive interconnection attributes of optics to provide a new approach to optical processing of sensory data.

UNCLASSIFIED

TABLE OF CONTENTS

	<u>Page</u>
1. INTRODUCTION	1
2. CURRENT PROGRESS	2
3. DISCUSSION AND NEW RESEARCH DIRECTIONS	4
4. LIST OF PUBLICATIONS, THESES AND OTHER ACTIVITIES	6
5. REFERENCES	8
6. APPENDICES	9
I. Polarization Effects in Microwave Diversity Imaging of Perfectly Conducting Cylinders . .	I-1
II. Microwave Diversity Imaging of Objects in The Presence of Severe Clutter	II-1
III. Optical Implementation of the Hopfield Model	III-1



Accession For	
NTIS	<input checked="" type="checkbox"/>
CRA&I	<input type="checkbox"/>
DTIC	<input type="checkbox"/>
TAB	<input type="checkbox"/>
Unannounced Justification	
By	
Distribution	
Availability Codes	
Dist	Avail and/or Special
A-1	

RESEARCH IN IMAGE UNDERSTANDING AS APPLIED TO
3-D MICROWAVE TOMOGRAPHIC AND PROJECTIVE IMAGING WITH NEAR OPTICAL RESOLUTION

1. INTRODUCTION

The objective of research under this grant is to achieve fundamental understanding of the dynamics of coherent and incoherent image formation and inverse scattering employing spectral, angular (aspect dependent) and polarization diversity as means for realizing cost-effective imaging of 3-D objects with near optical resolution. Special attention is to be given to 3-D microwave diversity radar imaging. The approach is Theoretical - through development of a unified theory of microwave diversity imaging for both stationary and non-stationary objects which has been reported on extensively in preceeding reports and, Experimental - through development and verification of methodologies for efficient microwave diversity imaging that can be employed in future broad-band imaging radar networks capable of providing 3-D projective or tomographic images of remote aerospace targets with near optical resolution.

To date unprecedented image resolution has been achieved (~ 1.5 cm) on scale models of relevant targets employing (6-17) GHz spectral window, polarization diversity, and ($\sim \pi/2$) angular aperture using a specially developed experimental microwave imaging facility for data acquisition and either Fourier inversion or an equivalent filtered back-projection reconstruction algorithm for image reconstruction. We expect the results of this effort to tell us how to achieve centimeter resolution on remote aerospace objects cost-effectively using microwave diversity radar networks that will also be ultimately capable of high speed automated target recognition and classification.

During the period of this report our research effort focused on: (a) the study of polarization and multiple scattering effects in microwave diversity imaging, (b) imaging in the presence of severe clutter, and (c) neural models for fault tolerant computing and robust signal processing and their optical implementation. Results of this research are summarized in Section 2 of this report with details being included in Section 6 as appendices. Discussion of research findings and of new research directions is given in Section 3. Lists of publications, theses, and other activities during the report period are given in Section 4.

2. CURRENT PROGRESS

To date our efforts have focused on the investigation of methods that enable the formation of highest resolution microwave and millimeter wave images of scattering bodies cost-effectively. At such high resolutions, the effect of multiple scattering in images of complex shaped scattering objects become particularly important as an image degrading mechanism or as an effect that its proper understanding and interpretation can convey additional information about the object. The effect of multiple scattering is to impose on the microwave image artefact or detail that makes it depart from the visually expected or "optical" image. For this reason, a systematic theoretical and experimental study of multiple scattering effects in the imaging of simple bodies e.g., consisting of two conducting or dielectric cylinders and the role played by polarization in such effects was conducted (See Appendix I for details). Analysis of multiple scattering effects between cylinders explained well the artefacts observed in earlier imaging experiments of such objects and their dependence on polarization of the

illuminating and receiving antennas. The advantage of using circularly polarized illumination and cross-polarized illuminating and receiving antennas to suppress such artefacts is demonstrated. This work also illustrates dramatically the power of microwave diversity imaging techniques as a tool in study and understanding of electromagnetic scattering.

Another task studied during the period of this report is evaluation of the capabilities of microwave diversity imaging in the formation of recognizable images in the presence of severe background clutter. This problem is important for certain modalities of radar imaging such as space-borne imaging of low-flying aircraft employing a "spot-light" imaging mode and imaging of internal structure of penetrable dielectric bodies in the presence of strong surface reflections. Details and results of this study are given in Appendix II. There a projection image of the visible scattering centers of a test object, a 72:1 metalized scale model of the space shuttle, was obtained employing a spectral window of 11 GHz (6.1-17.5 GHz) and an angular window of 90°. The shuttle model was imaged when situated 40 cm above corrugated aluminum ground planes of different roughness to simulate ground clutter from different terrain. Excellent polarization enhanced images of the target shape, clearly delineated above the image of the ground plane were obtained. These compare very well with flood-lit side-view photographs of the configuration showing the silhouette of the object. The results clearly demonstrate the advantages of using extended spectral and angular windows in this mode of imaging.

Another research task considered during this period was the study of neural models and their optical implementation for achieving associative memories that can be employed in robust fault-tolerant computing and information processing of sensory (radar, optical, infra-red, etc.) data. The results of optical implementation of a 32 neuron network and its

evaluation as an associative memory are detailed in Appendix III. An outer product storage algorithm, the so called Hopfield model, is employed to realize distributed information storage akin to holographic storage of information. This work demonstrates clearly the power of optics, namely parallelism and ease of making global or semi-global interconnection, in the implementation of simplified models of neural nets. On the other hand neural net modeling introduces the power of nonlinear feedback into optics to result in optical processors that can process sensory information collectively with a degree of robustness and fault tolerance that was not possible earlier.

3. DISCUSSION AND NEW RESEARCH DIRECTIONS

The principles and methodologies of microwave diversity imaging studied in our work show that it is possible to produce high resolution projection or tomographic images of radar targets with near optical resolution. Such images are perfectly suited for recognition by the eye-brain system. They have however several features that make them ideal for use in automated recognition schemes. These include: (a) the reconstructed image is always centered about the origin of the image plane. This is a direct consequence of the target derived reference method employed to produce synthetically during pre-processing of the collected data a phase reference point centered on the target. (b) the image is edge enhanced containing information about edges, protrusions and other characteristic detail necessary for recognition while all other detail such as flat surfaces that is not necessary for recognition is discarded. This represents a highly desirable reduction of the

dimensionality of the spatial signals being processed. Edge enhancement occurs naturally because of the specular nature of electromagnetic scattering from smooth surfaced man made objects and because of the range of wavelengths used (physical optics approximation). The process is analogous to the deliberate generation of a "primal sketch" of a gray level image as a first step in digital pattern recognition and machine vision except that it occurs naturally. (c) although the data (Fourier space slice) of the scattering object is collected by viewing the object (e.g., aero-space object) at a slant angle, the retrieved edge enhanced image appears as if the scattering object is being imaged directly from below. Such an image shows those scattering centers on the lower side of a target that scatter incident illumination back into the receiver (or receivers) used to measure the scattered field.

The above features of the image obtained in microwave diversity imaging are extremely helpful in feature extraction i.e., the generation of target classifiers that are distortion invariant. That is, classifiers that are scale, rotation, and position invariant. Accordingly, we have initiated a study of target classifiers. This includes a *sinogram* classifier in which the range-profile of the target measured at different aspects angles (i.e., different azimuthal angles, $0 \leq \phi \leq 2\pi$ at fixed elevation angle θ) are plotted in a rectangular format of range-profile vs. ϕ . A discrete visible scattering centers on the target describes a portion of sinusoidal trace in the sinogram presentation extending over the range of angles ϕ for which the scattering center is visible to the measuring system. The phase and amplitude of the sinusoidal trace depends on the relative position of the scattering center. Normalization by the maximum

amplitude and plotting the sinogram over $0 < \phi < 2\pi$. The data in the sinogram is exactly the same as the data in the image since one way of forming an image is by filtered back-projection [1] where the range profiles are plotted in polar format and backprojected to form the image by coherent addition of the contribution of the various back-projections at each point in the image plane. We expect sinogram classifiers to be of use as training sets for two-dimensional versions of the one-dimensional associative memory described in Appendix III. Such memories can be viewed then as "filters" that respond only if one of the entities stored in them or a close version of one of them (close in the Hamming sense) is used to stimulate or initialize the memory. In this fashion we would realize a rudimentary automated recognition system that is both robust and fault-tolerant providing thereby a new approach to automated radar target recognition.

4. LIST OF PUBLICATIONS, THESES AND OTHER ACTIVITIES

During the period of this report the following papers have been published or presented at national or international meetings:

1. N.H. Farhat, C.L. Werner and T.H. Chu, "Prospects of Three Dimensional Projective and Tomographic Imaging Radar Networks", Radio Science, Vol. 19, Sept./Oct. 1986, pp. 1347-1355.
2. N.H. Farhat, D. Psaltis, A. Prata and E. Paek, "Optical Implementation of the Hopfield Model", App. Optics, Vol. 24, May 1985, pp. 1469-1475.
3. N. Farhat, "Tomography and Inverse Scattering", Proc. ICO-13, 13th Congress of the International Commission on Optics, Sappora, Japan, 1984.
4. D. Psaltis and N. Farhat, "A New Approach to Optical Information Processing Based on the Hopfield Model", 13th Congress of the International Commission on Optics, ICO-13. Sapporo, Japan, 1984. Also published in Conference Digest.

5. N. Farhat and D. Psaltis, "Optical Implementation of the Hopfield Model", OSA Annual Meeting, San Diego, CA., Oct. 1984.
6. D. Psaltis and N. Farhat, "Optical Computing Based on the Hopfield Model", OSA Topical Meeting on Optical Computing, Lake Tahoe, March 1985.
N. Farhat and D. Psaltis, "Optical Implementation of the Hopfield Model", OSA Topical Meeting on Optical Computing, Lake Tahoe, March 1985.
7. N. Farhat, "Optical Implementations of Neural Networks", Workshop on Neural Network Models for Computing, Santa Barbara, CA., April 1985.
8. N.H. Farhat and Yuhshyen Shen, "Microwave Imaging of Objects in the Presence of Severe Clutter", Annual OSA Meeting, Wash. D.C., Oct. 1985.
9. N.H. Farhat, K.S. Lee and Li-Szu Chang, "High-Speed Fourier Camera", Annual OSA Meeting, Wash. D.C., Oct. 1985.
10. K.S. Lee and N.H. Farhat, "Content Addressable Memory with Smooth Transition and Adaptive Thresholding", Annual OSA Meeting, Wash. D.C., Oct. 1985.
11. N.H. Farhat and D. Psaltis, "Architectures for Optical Implementation of 2-D Content Addressable Memories", Annual OSA Meeting, Wash. D.C., Oct. 1985.
12. D. Psaltis, E. Paek, J. Hong, and N. Farhat, "An Acousto-Optic Implementation of Neural Network Models", Annual OSA Meeting, Wash. D.C., Oct. 1985.
13. D.L. Jaggard, K. Schultz, Y. Kim and P. Frangos, "Inverse Scattering for Dielectric Media", Annual OSA Meeting, Wash. D.C., Oct. 1985.

Invited Presentations

1. N. Farhat, "Tomographic Radar Imaging with Near Optical Resolution", Drexel University, Dept. of Electrical Engineering, Jan. 1985.
2. N. Farhat, "Tomographic Radar Imaging", AT&T Technology Systems and Bell Laboratories, National Engineering Week lecture series. Reading, PA, Feb. 1985.
3. N. Farhat, "Optical Processing for 3-D Tomographic Imaging Radar", Sigma Xi Initiation Dinner. Bucknell University, March 1985.
4. N. Farhat, "Optical Computing Implementation for Neural Processing in the Eye-Brain System", Computer Chapter, IEEE N.J. Coast Section Seminar, April 1985.
5. N. Farhat, "Neural Networks and Optical Computing", DARPA Briefing, April 1985.

Theses

- P.V. Frangos, "The Electromagnetic Inverse Scattering Problem For Layered Dispersionless Dielectrics", May 1985.
- K.I. Schultz, "Reconstruction Algorithms in Microwave Diffraction Imaging", May 1985.
- Y. Kim, "Accurate One-Dimensional Inverse Scattering Using a Nonlinear Renormalization Technique", Aug. 1985.

5. REFERENCES

1. N.H. Farhat, "Research in Image Understanding as Applied to 3-D Tomographic Imaging with Near Optical Resolution", University of Pennsylvania report EO/MO 7, prepared for the Air Force Office of Scientific Research, Nov. 1984.

6. APPENDICES

- I. Polarization Effects in Microwave Diversity Imaging of Perfectly Conducting Cylinders.
- II. Microwave Diversity Imaging of Objects in the Presence of Severe Clutter.
- III. Optical Implementation of the Hopfield Model.
(reprint)

APPENDIX I

POLARIZATION EFFECTS IN MICROWAVE DIVERSITY IMAGING OF PERFECTLY CONDUCTING CYLINDERS

Tah-Hsiung Chu
RCA David Sarnoff Research
Center
Rm 3-231, P.O. Box 432
Princeton, NJ 08540

Nabil H. Farhat
University of Pennsylvania
The Moore School of Electrical
Engineering
200 S. 33rd Street
Philadelphia, PA 19104

ABSTRACT

A theoretical vector development of the directly and mutually scattered wavefield of two cylinders in a bistatic measuring system is presented. The two scattered fields are shown to be polarization dependent, the images reconstructed from the directly or mutually scattered far field of each polarization include different features of the scattering object. An automated microwave imaging system employing frequency, polarization, and angular diversity is utilized to verify the theoretical results. Analytical and experimental results are shown to be in good agreement. The polarization effects of multiscatterers are also discussed. The results presented illustrate the utility of imaging methods in the study of electromagnetic scattering problems and in image understanding in general.

I. INTRODUCTION

The use of polarization diversity over an extremely broad spectrum in coherent scattering measurements as a means of acquiring more information about the scattering object has been the subject of extensive study at the Electro-Optics and Microwave-Optics Laboratory at the University of Pennsylvania [1-4]. An excellent review of the role of polarization in conveying useful information about the scatterer's characteristics is found in [5], and a discussion of the polarization effects and symmetry is given in [6]. In this paper the results of a detailed examination of polarization effects associated with the far field scattered from two conducting cylinders is presented. The influence of polarization on microwave images of the cylinders and on the occurrence of image artefact is determined analytically and verified experimentally.

A theoretical vector development of the far field scattered by perfectly conducting cylinders in a bistatic measuring system is derived in Section II. The approach is first to derive an expression for the field scattered from a single cylinder illuminated by a right-hand circularly polarized (RHCP) plane wave. This expression is then extended in Section III to the case of the directly scattered (or first order) field of two cylinders. The mutually scattered (or second order) field from two cylinders is then formulated in terms of a coherent summation of the scattered field from each cylinder due to the incident wave scattered from the other cylinder. Theoretically, one should proceed in this fashion to calculate the n -th order scattered field. However those higher order scattering terms are found to become negligibly small when the spacing between the two

cylinders is large compared to their radius and to the illuminating wavelength. Therefore in order to simplify computational tasks, only the second order scattered field is analytically derived in this paper. This is called the mutually scattered field. The total wavefield scattered by two cylinders becomes the coherent superposition of the directly scattered component and the mutually scattered component for each polarization. In Section IV, the use of an automated microwave imaging facility employing frequency, polarization and angular diversity to verify the results of theoretical analysis is described. The analytical and experimental results are shown to be in good agreement. The results show that depolarization effects in the mutually scattered field component are more pronounced than in the directly scattered component. Depolarization is taken to be the term describing the change of the polarization of an electromagnetic wave from one state to another brought about by the scattering process.

The notation used in describing the state of polarization in this paper is given next. Referring to Fig. 1, consider a plane containing the z-axis perpendicular to the plane of the paper and the incident wave vector \hat{k}_i . The quantities E_z^i and E_ϕ^i are orthogonal components of a linearly polarized incident plane wave lying respectively parallel and perpendicular to this plane. When right-hand and left-hand circularly polarized fields E_R^i (RHCP) and E_L^i (LHCP) are used they can be related to E_z^i and E_ϕ^i by [7],

$$\begin{bmatrix} E_R^i \\ E_L^i \end{bmatrix} = \frac{1}{\sqrt{2}} \begin{bmatrix} 1 & -j \\ 1 & j \end{bmatrix} \begin{bmatrix} E_z^i \\ E_\phi^i \end{bmatrix} \quad (1)$$

Similarly, we can express the right-hand E_R^s and left-hand E_L^s circularly

polarized components of the scattered field in terms of the scattered fields E_z^s and E_ϕ^s as

$$\begin{bmatrix} E_R^s \\ E_L^s \end{bmatrix} = \frac{1}{\sqrt{2}} \begin{bmatrix} 1 & -j \\ 1 & j \end{bmatrix} \begin{bmatrix} 1 & 0 \\ 0 & -1 \end{bmatrix} \begin{bmatrix} E_\phi^s \\ E_z^s \end{bmatrix} \quad (2)$$

$$= \frac{1}{\sqrt{2}} \begin{bmatrix} 1 & j \\ 1 & -j \end{bmatrix} \begin{bmatrix} E_\phi^s \\ E_z^s \end{bmatrix}$$

where the additional matrix $\begin{bmatrix} 1 & 0 \\ 0 & -1 \end{bmatrix}$ accounts for the coordinate system changing "polarization handedness" upon reflection from the scatterer. Furthermore, because of the change in "handedness", E_L^s and E_R^s will be called the co-polarized and cross-polarized (or depolarized) components of the scattered wavefield when the incident wave is RHCP namely E_R^i .

II. POLARIZATION EFFECTS IN SCATTERING FROM A SINGLE INFINITELY LONG CYLINDER

A. Formulation

Consider an infinitely long cylinder of radius a illuminated by a RHCP plane wave E_R^i as depicted in Fig. 1. The cylinder axis is in the z -direction. From eq. (1) the incident electric field can be expressed as

$$E_R^i = \frac{1}{\sqrt{2}} (E_\phi^i - jE_z^i) \quad (3)$$

where from [7,8],

$$E_z^i = E_0 e^{-jkR \cos(\phi_r - \phi_i)} \quad (4)$$

and

$$E_\phi^i = \frac{1}{j\omega\epsilon_0} (\nabla \times H_z^i \hat{z})_\phi \quad (5)$$

with

$$H_z^i = H_0 e^{-jkR \cos(\phi_r - \phi_i)} \quad (6)$$

are the parallel and perpendicular polarized components of the incident wave, $E_0 = \eta_0 H_0$, η_0 being the intrinsic impedance of free space, ϕ_i and ϕ_r are the angles between the x-axis and the directions of incidence and observation, and $\phi_r = \pi - \phi_i$ in a bistatic measurement system.

Equations (4) and (5) can be expressed in a Fourier-Bessel series as [7, 8],

$$E_z^i = E_0 \sum_{n=-\infty}^{\infty} (-j)^n J_n(kR) e^{jn(\phi_r - \phi_i)} \quad (7)$$

$$H_z^i = H_0 \sum_{n=-\infty}^{\infty} (-j)^n J_n(kR) e^{jn(\phi_r - \phi_i)} \quad (8)$$

where $J_n(x)$ is the Bessel function of the first kind of order n , and E_0 and H_0 are the electric and magnetic field amplitudes of the incident plane wave.

The scattered wavefield components E_z^s and E_ϕ^s determined from the boundary conditions,

$$(-j E_z^i + E_z^s) \Big|_{R=a} = 0 \quad (9)$$

and

$$(E_{\phi}^i + E_{\phi}^s) \Big|_{R=a} = \frac{1}{j\omega\epsilon_0} [\nabla X(H_z^i + H_z^s) \hat{z}]_{\phi} \Big|_{R=a} = 0 \quad (10)$$

where R designates radial distance (see Fig. 1), are given by,

$$E_z^s = jE_0 \sum_n (-j)^n \frac{J_n(ka)}{H_n^{(2)}(ka)} H_n^{(2)}(kR) e^{jn(\phi_r - \phi_i)} \quad (11)$$

and

$$E_{\phi}^s = -jE_0 \sum_n (-j)^n \frac{J_n'(ka)}{H_n^{(2)}(ka)} H_n^{(2)}(kR) e^{jn(\phi_r - \phi_i)} \quad (12)$$

where the summations over n here and in subsequent equations is understood to range from $-\infty$ to ∞ , $H_n^{(2)}(x)$ is the Hankel function of the second kind, and $H_n^{(2)'}(x)$ is its derivative with respect to the argument x .

If $kR \gg 1$, i.e., under the far field approximation, the bistatic scattered field ($\phi_i \neq 0$, and $\phi_r = \pi - \phi_i$) becomes

$$E_z^s = j \sqrt{\frac{2j}{\pi kR}} e^{-jkR} E_0 \sum_n \frac{J_n(ka)}{H_n^{(2)}(ka)} e^{jn(\pi - 2\phi_i)} \quad (13)$$

$$E_{\phi}^s = - \sqrt{\frac{2j}{\pi kR}} e^{-jkR} E_0 \sum_n \frac{J_n'(ka)}{H_n^{(2)}(ka)} e^{jn(\pi - 2\phi_i)} \quad (14)$$

Using the transform relationship given in eq. (2), the scattered fields expressed in terms of circular polarization are

$$\begin{aligned}
E_R^S &= \frac{1}{\sqrt{2}} (E_\phi^S + jE_z^S) \\
&= \sqrt{\frac{j}{\pi k R}} e^{-jkR} E_0 \sum_n \left(-\frac{J_n'(ka)}{H_n^{(2)}(ka)} - \frac{J_n(ka)}{H_n^{(2)}(ka)} \right) e^{jn(\pi-2\phi_i)} \quad (15)
\end{aligned}$$

and

$$\begin{aligned}
E_L^S &= \frac{1}{\sqrt{2}} (E_\phi^S - jE_z^S) \\
&= \sqrt{\frac{j}{\pi k R}} e^{-jkR} E_0 \sum_n \left(-\frac{J_n'(ka)}{H_n^{(2)}(ka)} + \frac{J_n(ka)}{H_n^{(2)}(ka)} \right) e^{jn(\pi-2\phi_i)} \quad (16)
\end{aligned}$$

Equations (15) and (16) indicate that the far field scattered from a cylinder illuminated by a RHCP plane wave is elliptically polarized in the bistatic case and also in the monostatic scattering case ($\phi_i=0$ and $\phi_r=\pi$) because E_z^S and E_ϕ^S in eqs. (13) and (14) differ in magnitude and are not in phase. The observed scattered far field, measured for example by a coherent receiver, can be separated into two parts: one containing the range term $\exp(-jkR)/\sqrt{R}$ appearing outside the summation terms which accounts for the propagation time delay or phase shift from the coordinate origin to the receiver; and the summation terms which can be viewed as the equivalent to the "Bojarski identity" [9,10] which strictly speaking conveys information about the object in the high frequency limit ($ka \gg 1$).

It was shown by Bojarski and Lewis assuming physical optics and Born approximations hold and neglecting polarization effects, that a Fourier transform relationship exists between the shape of a perfectly conducting object and its range-corrected backscattered far field frequency response. In the next section, numerical examples are given to examine and elucidate

the Fourier inversion reconstruction for each of the circularly polarized fields given in eqs. (15) and (16) in the microwave regime. Note that in arriving at the results in eqs. (15) and (16) the physical optics approximation was not involved and hence they hold for any value of the wavenumber k .

B. Numerical Results

The range-corrected scattered far field component E_L^s and E_R^s were calculated from the summation terms in eqs. (15) and (16) using 33 terms for n ranging from -16 to 16 for the frequency range (6-17) GHz for a cylinder of radius 3.8 cm and a bistatic angle of $\phi_1 = 6^\circ$. The results are shown in Fig. 2(a) and (b). The spectral range (6-17) GHz is chosen to coincide with the measurement capabilities of the system utilized in the experimental portion of the study. The depolarized component E_R^s of the scattered field is shown to be about 25dB lower than the co-polarized component E_L^s and is seen to decrease as the frequency approaches the optical regime [11].

One-dimensional Fourier inversion of the range-corrected E_L^s component with respect to k gives the range profile of the illuminated cylinder shown in Fig. 2(c). The peak in the profile corresponds to specular reflection from the front surface of the cylinder. The range profile reconstructed from the range-corrected depolarized component E_R^s shown in the same figure is seen, however, to contain two peaks. The first peak is caused also by specular reflection from the front surface of the cylinder, while the second peak which is about 20dB weaker is due to the effect of creeping wave associated with the surface wave propagating around the cylinder [7]. The contribution from the creeping wave is known also to decrease as the cylinder radius increases.

Since the range resolution is inversely proportional to the spectral range of the illuminating signal, the ability to pinpoint the reflection location on the scattering cylinder is greatly enhanced by gathering data over a broad frequency range. A long cylinder can therefore be used as a calibration object for characterizing broadband microwave scattering system used in frequency and polarization diversity measurement [4]. In Section IV, the scattered field E_R^s and E_L^s from two cylinders will be measured in an anechoic chamber using a single cylinder as the calibration object for system characterization.

III. POLARIZATION EFFECTS IN SCATTERING FROM TWO INFINITELY LONG CYLINDERS

A. Formulation of Direct Scattering

The directly scattered wavefield from two conducting infinitely long parallel cylinders illuminated by a RHCP plane wave as shown in Fig. 3 can be obtained by superposition using eqs. (11) and (12). This leads to a summing of eqs. (11) and (12) with each multiplied by a phase term due to the offset distance b from the coordinate origin to each cylinder. The resultant field expressions referring to the quantities shown in Fig. 3

$$\begin{aligned}
 l_{E_z}^s &= l_{E_z^+}^s + l_{E_z^-}^s \\
 &= j E_0 \sum_n (-j)^n \left\{ \frac{J_n(ka)}{H_n^{(2)}(ka)} [H_n^{(2)}(kR_+) e^{jn(\phi_+ - \phi_i)} e^{-jkb \cos(\theta_+ - \phi_i)} \right. \\
 &\quad \left. + H_n^{(2)}(kR_-) e^{jn(\phi_- - \phi_i)} e^{jkb \cos(\theta_- - \phi_i)}] \right\} \quad (17)
 \end{aligned}$$

and

$$1_{E\phi}^s = 1_{E\phi}^s + 1_{E\phi}^s$$

$$= -j E_0 \sum_n \{ (-j)^n \frac{J_n'(ka)}{H_n^{(2)}(ka)} [H_n^{(2)}(kR_+) e^{jn(\phi_+ - \phi_i)} e^{-jkb \cos(\theta_{\rightarrow} - \phi_i)} + H_n^{(2)}(kR_-) e^{jn(\phi_- - \phi_i)} e^{jkb \cos(\theta_{\rightarrow} - \phi_i)}] \} \quad (18)$$

where the superscript 1 is used here to designate the direct scattering, as the superscript 2 will be used later to designate the doubly scattered field or mutual scattering case. The subscripts + and - are used to distinguish the two cylinders and θ_{\rightarrow} is the angle between the line connecting the centers of the two cylinders and the x-axis.

In the far field approximation, $kR \gg 1$, we can use the following approximations

$$\begin{aligned} R_+ &\sim R + b \cos(\theta_{\rightarrow} + \phi_i) \\ R_- &\sim R - b \cos(\theta_{\rightarrow} + \phi_i) \end{aligned} \quad (19)$$

and

$$\phi_- \sim \phi_+ \sim \pi - \phi_i \quad (20)$$

Therefore, after normalizing the range term $\exp(-jkR)/\sqrt{R}$, eqs. (17) and (18) become

$$1_{E_z}^s = j \sqrt{\frac{2j}{\pi k}} 2E_0 \cos(2kb \cos\theta_{\rightarrow} \cos\phi_i) \sum_n \frac{J_n(ka)}{H_n^{(2)}(ka)} e^{jn(\pi - 2\phi_i)} \quad (21)$$

$$l_{E_{\phi}}^s = - \sqrt{\frac{2j}{\pi k}} 2E_0 \cos(2kb \cos\theta_{-+} \cos\phi_i) \sum_n \frac{J'_n(ka)}{H'_n(2)(ka)} e^{jn(\pi-2\phi_i)} \quad (22)$$

or

$$l_{E_R}^s = 2 \cos(2kb \cos\theta_{-+} \cos\phi_i) E_R^s \quad (23)$$

$$l_{E_L}^s = 2 \cos(2kb \cos\theta_{-+} \cos\phi_i) E_L^s \quad (24)$$

where E_R^s and E_L^s are the expressions for the scattered fields from one cylinder as given by eqs. (15) and (16) excluding the range terms. Eqs. (23) and (24) are equal to eqs. (15) and (16) (excluding the range term) multiplied by a sum of two linear phase terms contributed from the projected distances $\pm b \cos\theta_{-+} \cos\phi_i$ from each cylinder to the coordinate origin.

B. Numerical Results

Figure 4 shows the range profiles derived from the LHCP and the RHCP components of the directly scattered field for the case of $\theta_{-+} = 0^\circ$ and $a=3.8\text{cm}$, $b=13.7\text{cm}$. These are near replicas of single cylinder profiles displaced by distance $\pm b \cos\phi_i$.

By measuring the backscattered field components for different closely spaced values of θ_{-+} , correcting them for the range factor $\exp(-jkR)/\sqrt{R}$, and presenting them in polar format in which the polar angle is θ_{-+} and radial distance represents frequency, we can obtain a slice in the Fourier space of the object [3,4]. Fourier inversion of the slice data after interpolation onto a rectangular format using a four nearest neighbor interpolation algorithm [12] yields in accordance to the projection-slice

theorem [13] a projection image representing the projection of the scattering centers of the object on a plane parallel to the plane of the Fourier space slice.

Figure 5(a) and (b) shows Fourier plane slices obtained from the ${}^1E_L^s$ and ${}^1E_R^s$ components presented in a polar format consisting of 256 radial lines equally spaced over 360° , with each line containing 64 equally spaced frequency points covering (6-17) GHz range. Considering that the radial (frequency) and angular (aspect) sampling criterion needed to avoid aliasing are respectively $\delta f \simeq c/4b$ and $\delta \theta \simeq \lambda_{\min}/2b$ [4], the acquired data in the above polar format is somewhat oversampled. The reconstructed images for each circularly polarized component as obtained via a two-dimensional Fourier transformation, are given in Fig. 6. Several observations can be made based on the images shown. First, the ${}^1E_L^s$ component gives two distinct circles representing the external cross-sectional outline images of the two cylinders. The radii and spacings of the cylinders in the two images correspond quite closely to the values a and b of the object. This result agrees with the physical optics diffraction theory given by Bojarski and Lewis in the context of their inverse scattering theory [9,10]. However the ${}^1E_R^s$ component, ignored in the scalarized physical optics approximation, also gives two faint circles which are contributed from the weak depolarization and creeping wave effects. In the next section, we will analyze the mutual scattering between two cylinders in each polarization state.

C. Formulation of Mutual Scattering

First we consider the case when the "-" cylinder is illuminated by the directly scattered wave from "+" cylinder to obtain the contribution

of the "-" cylinder to the second order mutually scattered wavefield. The contribution of the "+" cylinder to the mutually scattered wave by re-scattering the directly scattered wave from "-" cylinder can be obtained by interchanging the "+" and "-" subscripts in the resulting expressions.

The scattered wave from the "+" cylinder incident on the "-" cylinder is rewritten from the first terms in eqs. (17), (18) and (5) as

$$\begin{matrix} 2 \\ - \end{matrix} E_z^i = \begin{matrix} 1 \\ + \end{matrix} E_z^s = \sum_n \begin{matrix} 1 \\ + \end{matrix} A_n H_n^{(2)}(kR_+) e^{jn\phi_+} \quad (25)$$

$$\begin{matrix} 2 \\ - \end{matrix} H_z^i = \begin{matrix} 1 \\ + \end{matrix} H_z^s = \sum_n \begin{matrix} 1 \\ + \end{matrix} B_n H_n^{(2)}(kR_+) e^{jn\phi_+} \quad (26)$$

where

$$\begin{matrix} 1 \\ + \end{matrix} A_n = jE_0 (-j)^n \frac{J_n(ka)}{H_n^{(2)}(ka)} e^{-jkb \cos(\theta_+ - \phi_1)} e^{-jn\phi_1} \quad (27)$$

$$\begin{matrix} 1 \\ + \end{matrix} B_n = -H_0 (-j)^n \frac{J'_n(ka)}{H_n^{(2)}(ka)} e^{-jkb \cos(\theta_+ - \phi_1)} e^{-jn\phi_1} \quad (28)$$

where R_+ in accordance to Fig. 3 is now the distance between the center of the "+" cylinder and an observation point on the surface of the second cylinder. The second order mutually scattered wavefield from the "-" cylinder can then be expressed in terms of the cylindrical wave function [7,8] as

$$\begin{matrix} 2 \\ - \end{matrix} E_z^s = \sum_n \begin{matrix} 2 \\ - \end{matrix} A_n H_n^{(2)}(kR_-) e^{jn\phi_-} \quad (29)$$

and

$$\begin{matrix} 2 \\ - \end{matrix} H_z^s = \sum_n \begin{matrix} 2 \\ - \end{matrix} B_n H_n^{(2)}(kR_-) e^{jn\phi_-} \quad (30)$$

where the scattering coefficients 2A_n and 2B_n are determined from the boundary conditions

$$\left. \frac{{}^2E_i}{-z} + \frac{{}^2E_s}{-z} \right|_{R_-=a} = \sum_m \frac{{}^1A_m}{+} H_m^{(2)}(kR_+) e^{jm\phi_+} + \sum_n \frac{{}^2A_n}{-} H_n^{(2)}(kR_-) e^{jn\phi_-} \Big|_{R_-=a} = 0 \quad (31)$$

and

$$\left. \frac{{}^2E_i}{-\phi} + \frac{{}^2E_s}{-\phi} \right|_{R_-=a} = \frac{1}{j\omega\epsilon_0} [\nabla \times (\sum_m \frac{{}^1B_m}{+} H_m^{(2)}(kR_+) e^{jm\phi_+} + \sum_n \frac{{}^2B_n}{-} H_n^{(2)}(kR_-) e^{jn\phi_-}) \hat{z}] \Big|_{R_-=a} = 0 \quad (32)$$

and in using eqs. (25) and (26) to write eqs. (31) and (32) we have changed the summation variable from n to m .

In order to impose the boundary conditions at $R_-=a$, the term $H_m^{(2)}(kR_+)$ must be expressed in terms of the cylindrical wave referred to the coordinate of the "-" cylinder. Using the additional theorem [14], which is valid for $2b>a$, we can obtain

$$H_m^{(2)}(kR_+) e^{jm\phi_+} = \sum_n H_{n-m}^{(2)}(2kb) J_n(kR_-) e^{jn\phi_-} e^{-j(n-m)\theta_{-+}} \quad (33)$$

Substituting eq. (33) into eqs. (31) and (32) and equating the coefficients of $\exp(-jn\phi_-)$ to zero, the mutual scattering coefficients,

$$\frac{2}{-}A_n = - \frac{J'_n(ka)}{H_n^{(2)}(ka)} \sum_m \frac{1}{+}A_m H_{n-m}^{(2)}(2kb) e^{-j(n-m)\theta_{-+}} \quad (34)$$

and

$$\frac{2}{-}B_n = - \frac{J'_n(ka)}{H_n^{(2)}(ka)} \sum_m \frac{1}{+}B_m H_{n-m}^{(2)}(2kb) e^{-j(n-m)\theta_{-+}} \quad (35)$$

are found where $\frac{1}{+}A_m$ and $\frac{1}{+}B_m$ are given in eqs. (27) and (28). Note eq. (34) which is the scattering coefficient of the $\frac{2}{-}E_z^s$ component is the same as that derived by Twersky [15] for the second order scalar scattering coefficient of two cylinders. The other scattering coefficient $\frac{2}{-}B_n$ in eq. (35) belongs to the $\frac{2}{-}E_\phi^s$ component of the mutually scattered field from "-" cylinder and reflects for the vector formulation developed here.

Therefore

$$\begin{aligned} \frac{2}{-}E_z^s &= -jE_o e^{-jkb \cos(\theta_{-+} - \phi_i)} \sum_n \frac{J'_n(ka)}{H_n^{(2)}(ka)} H_n^{(2)}(kR_-) e^{jn\phi_-} \\ &\quad \sum_m (-j)^m \frac{J'_m(ka)}{H_m^{(2)}(ka)} e^{-jm\phi_i} H_{n-m}^{(2)}(2kb) e^{-j(n-m)\theta_{-+}} \end{aligned} \quad (36)$$

and

$$\begin{aligned} \frac{2}{-}H_z^s &= H_o e^{-jkb \cos(\theta_{-+} - \phi_i)} \sum_n \frac{J'_n(ka)}{H_n^{(2)}(ka)} H_n^{(2)}(kR_-) e^{jn\phi_-} \\ &\quad \sum_m (-j)^m \frac{J'_m(ka)}{H_m^{(2)}(ka)} e^{-jm\phi_i} H_{n-m}^{(2)}(2kb) e^{-j(n-m)\theta_{-+}} \end{aligned} \quad (37)$$

As $kr \gg 1$, the range-corrected scattered far field from the "-" cylinder due to the incoming wave from the "+" cylinder for each linear polarization will be,

$$\begin{aligned} {}^2_{-}E_z^s = & -j \sqrt{\frac{2j}{\pi k}} e^{-j2kbs \sin \phi_i \sin \theta} \rightarrow E_0 \sum_n \sum_m (-j)^{n+m} \frac{J_n(ka) J_m(ka)}{H_n^{(2)}(ka) H_m^{(2)}(ka)} \\ & e^{-j(n+m)\phi_i} H_{n-m}^{(2)}(2kb) e^{-j(n-m)\theta} \rightarrow \end{aligned} \quad (38)$$

and

$$\begin{aligned} {}^2_{-}E_\phi^s = & \frac{1}{j\omega\epsilon_0} (\nabla \times {}^2_{-}E_z^s \hat{z})_\phi \\ = & \sqrt{\frac{2j}{\pi k}} e^{-j2kbs \sin \phi_i \sin \theta} \rightarrow E_0 \sum_n \sum_m (-j)^{n+m} \frac{J'_n(ka) J_m(ka)}{H_n^{(2)}(ka) H_m^{(2)}(ka)} \\ & e^{-j(n+m)\phi_i} H_{n-m}^{(2)}(2kb) e^{-j(n-m)\theta} \rightarrow \end{aligned} \quad (39)$$

By interchanging the subscripts "+" and "-" in eqs. (38) and (39), we can obtain the mutually scattered far fields ${}^2_{+}E_z^s$ and ${}^2_{+}E_\phi^s$ from "+" cylinder due to the incoming wave or directly scattered from the "-" cylinder. The mutually scattered field from two cylinders for each linear polarization is the summation of these two terms i.e.,

$$^2E_z^s = ^2E_z^s + ^2E_z^s$$

$$= -j \sqrt{\frac{2j}{\pi k}} E_0 \sum_n \sum_m (-j)^{n+m} \frac{J_n(ka) J_m(ka)}{H_n^{(2)}(ka) H_m^{(2)}(ka)} e^{-j(n+m)\phi_i - j(n-m)\theta_{\rightarrow}}$$

$$H_{n-m}^{(2)}(2kb) \begin{cases} 2 \cos(2kb \sin\phi_i \sin\theta_{\rightarrow}) & \text{---- } n+m \text{ even} \\ -j2 \sin(2kb \sin\phi_i \sin\theta_{\rightarrow}) & \text{---- } n+m \text{ odd} \end{cases} \quad (40)$$

and

$$^2E_{\phi}^s = ^2E_{\phi}^s + ^2E_{\phi}^s$$

$$= \sqrt{\frac{2j}{\pi k}} E_0 \sum_n \sum_m (-j)^{n+m} \frac{J'_n(ka) J'_m(ka)}{H_n^{(2)}(ka) H_m^{(2)}(ka)} e^{-j(n+m)\phi_i - j(n-m)\theta_{\rightarrow}}$$

$$H_{n-m}^{(2)}(2kb) \begin{cases} 2 \cos(2kb \sin\phi_i \sin\theta_{\rightarrow}) & \text{---- } n+m \text{ even} \\ -j2 \sin(2kb \sin\phi_i \sin\theta_{\rightarrow}) & \text{---- } n+m \text{ odd} \end{cases} \quad (41)$$

From which the circular polarization expression,

$$^2E_R^s = (^2E_{\phi}^s + j^2E_z^s)/\sqrt{2} \quad (42)$$

and

$$^2E_L^s = (^2E_{\phi}^s - j^2E_z^s)/\sqrt{2} \quad (43)$$

can be obtained. Also here, because of the unequal magnitude and phase angle of the RHCP and LHCP scattered components in the above equations, the mutually scattered far field $^2E^s$ from two conducting cylinders illuminated with RHCP plane wave is elliptically polarized.

It is interesting to note that eqs. (38) and (39) have leading phase terms $\exp(j2kbsin\phi_i \sin\theta_{\rightarrow})$. This implies that contributions to the image reconstructed from ${}^2_{-}E^s$ (or ${}^2_{+}E^s$) will have an additional displacement $bsin\phi_i$ (or $-bsin\phi_i$) in the y-direction. The resulting image detail can be useful therefore in some applications for determining the bistatic scattering angle, if it is not known, from the received scattered far field of a two-cylinder object.

It can be seen that the second order scattering coefficients consist of sums of products of two scattering coefficients of the single cylinder and terms depending on the distance between the two cylinders. This mutually scattered far field expression can be then physically interpreted as arising from two scattering processes as the incident plane wave is doubly scattered by one cylinder onto the other and back. The second order scattering coefficient will approach zero for large separation between the two cylinders due to the behavior of the Hankel function $H_{n-m}^{(2)}(2kb)$. This implies the higher order scattering coefficients could be neglected when the cylinder spacing is large compared to the illuminating wavelength.

In the next section we will examine the mutual scattering of two cylinders for each polarization using numerical simulation.

D. Numerical Results

Shown in Fig. 7 is the mutually scattered field components ${}^2_{E_L}^s$ and ${}^2_{E_R}^s$ calculated from eqs. (42) and (43) for aspect angle $\theta_{\rightarrow} = 90^\circ$ with n and m in the summations ranging from -16 to 16. The magnitude of the depolarized component ${}^2_{E_R}^s$ is seen to be up to about 15dB greater than that of ${}^2_{E_L}^s$ due to the effect of the mutual scattering between the two cylinders. The corresponding range profiles reconstructed from each polarization component are

given in Fig. 7(c). Each of these shows two primary peaks whose separation is related to the bistatic angle ϕ_i . In addition the profile derived from the ${}^2E_L^s$ component shows additional weaker peaks and also the higher order terms ignored in our analysis. The value of $\phi_i = 6^\circ$ is used and those of a and b are as before.

The numerically generated Fourier space slices obtained by computing ${}^2E_R^s$ and ${}^2E_L^s$ as a function of frequency and rotation angle $\theta_{\rightarrow+}$ are shown in Fig. 8. The same polar format used earlier i.e., 64 equally spaced frequency points covering the range (6-17) GHz per radial line and 256 radial lines covering an angular range of 360° , is utilized. The images obtained by Fourier inversion of these slices are shown in Fig. 9. The reconstructed images exhibit the effect of mutual scattering between two cylinders. The effect consists of two symmetrical "smile patterns" with width $2(b-a)$. The two peaks presented in Fig. 7 correspond to a cross-sectional view of the "smile pattern" at $\theta_{\rightarrow+} = 90^\circ$. The lip separation, given by $b\sin\phi_i$, is determined by the bistatic angle. It becomes wider as the bistatic angle increases as indicated in Fig. 9(c) for which the bistatic angle ϕ_i is 8° as compared to $\phi_i = 6^\circ$ in (a) and (b) of the figure. The smile pattern will merge into a "ring pattern" as shown in Fig. 9(d) when $\phi_i = 0^\circ$ i.e., the case of monostatic scattering. This suggests that the bistatic angle spanned by transmitting and receiving antennas can, if necessary, in certain situations be determined from the lip separation of the cross-polarized image of a two cylinder test target.

The total scattered wavefield from two cylinders is the superposition of directly scattered components given in eqs. (23), (24) and the mutually scattered components given in eqs. (42), (43) for each state of polarization. Fourier space slices, obtained from the computed total RHCP and LHCP

components, and their reconstructed images are shown in Fig. 10. Due to the pronounced depolarization effect contributed from the mutual scattering, the RHCP component dominated by the $^2E_R^s$ wavefield, is about up to 15dB greater than $^1E_R^s$. Therefore the reconstructed image consists of two distinct image of the smile pattern bridging two adjacent faint circles representing the projection image of the two cylinders. The slight spacing at the corners of the "smile pattern", as compared to the narrower spacing in the experimental results presented in the following section, is attributed to the finite number of terms taken in the calculation of eqs. (40) and (41). The LHCP component gives the same image as Fig. 6(a) of the directly scattered data which is merely the projection of the two cylinders because for this case $^2E_L^s$ is more than 20dB weaker than $^1E_L^s$ and hence this image is seen to be free of any depolarization effects. Note in the strict sense of imaging, the "smile patterns" in Fig. 9 do not correspond to any physical detail of the two cylinders and hence represent "ghost images" or image artefact.

IV. EXPERIMENTAL RESULTS

Due to continuing advances in microwave instrumentation and technology, it is now possible to develop efficient and highly accurate computer-controlled microwave measurement system capable of collecting full vector information of the scattered wavefield including amplitude, phase, frequency and polarization [1-4]. The experimental arrangement used to acquire wideband polarization-selective scattering data of test objects is shown in Fig. 11. The test object, consisting of two metallic cylinders 27.4 cm apart, each 100 cm long and 3.8 cm in radius, is mounted on a computer controlled positioner situated in an anechoic chamber. The

entire measurement sequence consisting of angular positioning of the test object in azimuth in increments of 1.4° , incremental frequency stepping over a (6-17) GHz spectral range, switching of antenna polarization, digitization and storage of the amplitude and phase of the scattered field measured by the coherent receiver, is carried out under computer control which also performs the required digital signal processing. As mentioned earlier in Section II, a single metallic cylinder is used to characterize the system frequency response including determination of the range information needed to correct for the range term. Further detail on this and on the removal of clutter signals in anechoic chamber measurements are found in [3,4].

Results of two circular polarization measurements, shown in Fig. 12, are obtained with the system using RHCP plane wave illumination produced by a parabolic reflector antenna and an electronically switchable RHCP and LHCP dual-polarization horn receiving antenna. The Fourier slice data and corresponding reconstructed images for each measured polarization are shown. Several observations can be made. First, both the RHCP and LHCP scattered fields and their reconstructed images agree well with the analytical results given in Fig. 10. Secondly, the RHCP component gives a distinctive image of the "smile pattern" and two faint circles. This experimental result shows that the higher order scattering terms, beyond $-16 < n < 16$ used in our computations, are negligibly small when the cylinders spacing is chosen to be greater than the radius of each cylinder and than the illuminating wavelength. Thirdly, the depolarized image of $^2E_L^s$ is nearly not visible because it is 40db lower in image intensity (corresponding to 20dB weaker amplitude) than the $^1E_L^s$ component.

V. DISCUSSION

In an attempt to clarify the role of polarization diversity in microwave image formation, a systematic analytical and experimental study of the directly and mutually scattered wavefields of two cylinders in an orthogonal polarization basis was undertaken. The results show that the analytical and experimental results obtained and reported here are in good agreement. These results suggest that in the case of dual-cylinder objects illuminated with a RHCP plane wave, the LHCP scattered field primarily determined by specular reflections from the illuminated surfaces of cylinders is free of any noticeable depolarization effects arising from multiple scattering between the two cylinders. Two-dimensional Fourier inversion of the LHCP Fourier slice data gives a projection image showing the shape and location of scattering centers on the two cylinders. Thus RHCP plane wave illumination and LHCP scattered field measurement can be used to suppress multiple scattering effects, and therefore artefacts, in microwave imaging of cylinders and other more complex multiple segment objects. The RHCP measurement, on the other hand, gives the mutual scattering information. The image information in this case is an "artefact" as it does not correspond to any actual physical detail or optical image of the object. The mutual scattering information carries further detail about the scatterers and the scattering geometry. For example as shown here the artefact image detail can be related to the bistatic angle and the cylinder spacing.

The results presented here lead to better understanding of the role of polarization in microwave imaging in conveying more information about multiple simple-body scatterers e.g., cylinders considered here, and more complex objects in general. The methods presented also serve to illustrate

the power of microwave imaging techniques in the analysis and understanding of electromagnetic scattering problems.

VI. ACKNOWLEDGEMENT

The authors wish to thank C.L. Werner and R.E. Marx for their interest and useful discussion. This research was supported by the Air Force Office of Scientific Research, Air Force Systems Command, under grant no. AFOSR-81-0240F, the Army Research Office, under grant DAAG-29-83-K-0120 PO2 and the RCA Corporation.

References

- [1] C. L. Werner, "An Automated Frequency Response and Radar Cross-Section Measurement Facility for Microwave Imaging", Master Thesis, University of Pennsylvania, 1980
- [2] T. H. Chu, "Optimal Methodologies in Inverse Scattering Utilizing Wavelength, Polarization and Angular Diversity", Ph.D Dissertation, University of Pennsylvania, 1983
- [3] N. H. Farhat, C. L. Werner and T. H. Chu, "Prospects for Three-dimensional Projective and Tomographic Imaging Radar Network", Radio Science, Vol.19, No.5, Sep.-Oct. 1984, pp.1347-1355
- [4] N. H. Farhat and T. H. Chu, "Projection Image of 3-D microwave Scatterers with Near Optical Resolution" in Indirect Imaging, J. A. Robert Ed., Cambridge University Press, 1984, pp.33-40
- [5] W-M. Boerner, "Polarization Utilization in Electromagnetic Inverse Scattering", Ch.7 in Inverse Scattering Problems in Optics, H. P. Baltes, Ed., Vol.20, New York:Springer Verlag, 1980
- [6] G. E. Heath, "Bistatic Scattering Reflection Asymmetry, Polarization Reversal Asymmetry, and Polarization Reversal Reflection Symmetry", IEEE trans. on Antennas and Propagation, Vol.AP-29, No.3, May 1981, pp.429-434
- [7] G. T. Ruck, D. E. Barrick, W. D. Stuart and C. K. Krichbaum, Radar Cross Section Handbook, Ch.4, Vol.1, New York:Plenum 1970
- [8] R. F. Harrington, Time-Harmonic Electromagnetic Fields, Ch.5, New York: McGraw-Hill 1961
- [9] N. N. Bajarski, "Three-Dimensional Electromagnetic Short Pulse Inverse Scattering", Syracuse University Res. Corp., Syracuse, N.Y., Feb. 1967
- [10] R. M. Lewis, "Physical Optics Inverse Diffraction", IEEE trans. on Antennas and Propagation, Vol.AP-17, No.3, May 1969 pp.308-314
- [11] T. M. Smith and S. L. Borison, "Depolarization of a Circularly Polarized Wave by an Infinite Cylinder", IEEE trans. on Antennas and Propagation, Vol.AP-22, No.6, Nov. 1974, pp.796-798
- [12] R. M. Mersereau and A. V. Oppenheim, "Digital Reconstruction of Multi-dimensional Signals from Their Projections", Proc. of the IEEE, Vol.62, No.10, 1974, pp.1319-1338
- [13] G. T. Herman Ed., Image Reconstruction from Projections Implementation and Applications, Topics in Applied Physics, Vol.32, New York:

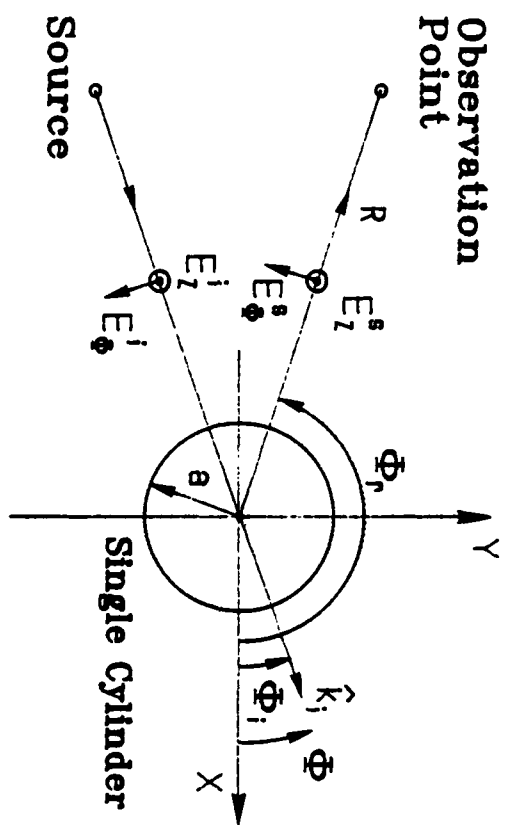
Springer-Verlag, 1979

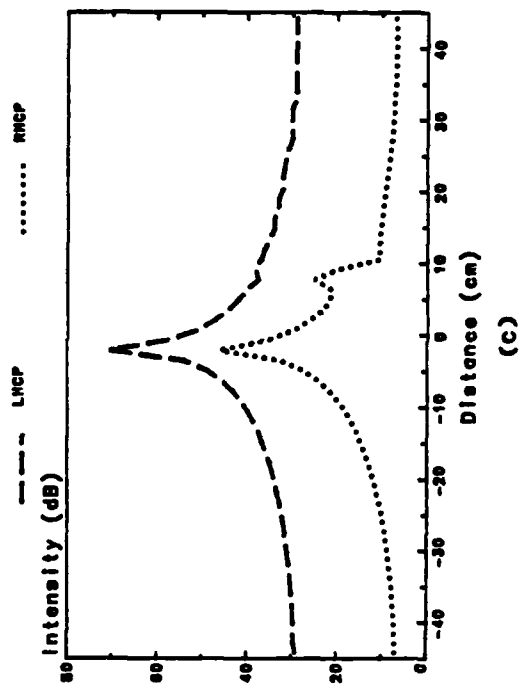
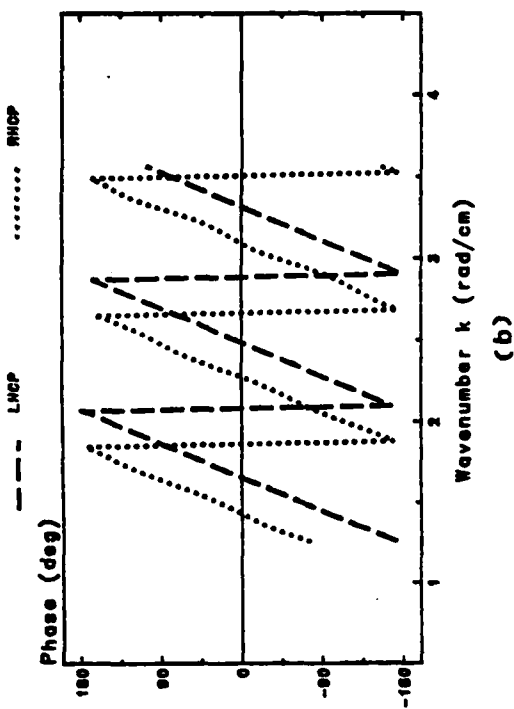
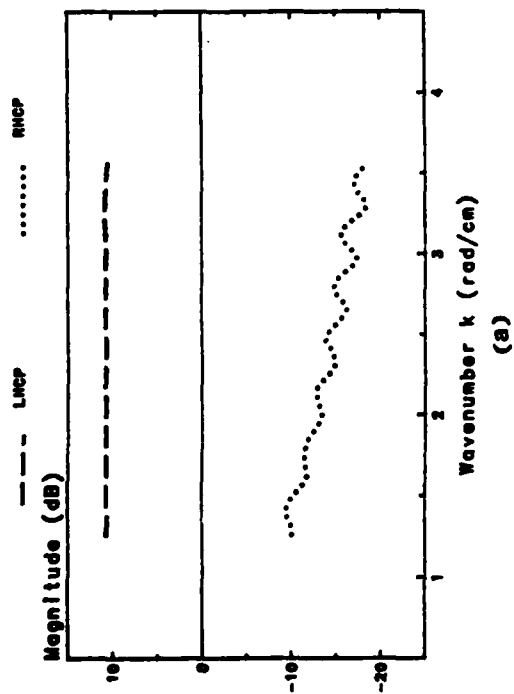
[14] G. N. Watson, A Treatise on the Theory of Bessel Functions, Cambridge University Press. Ch.11, London, 1958

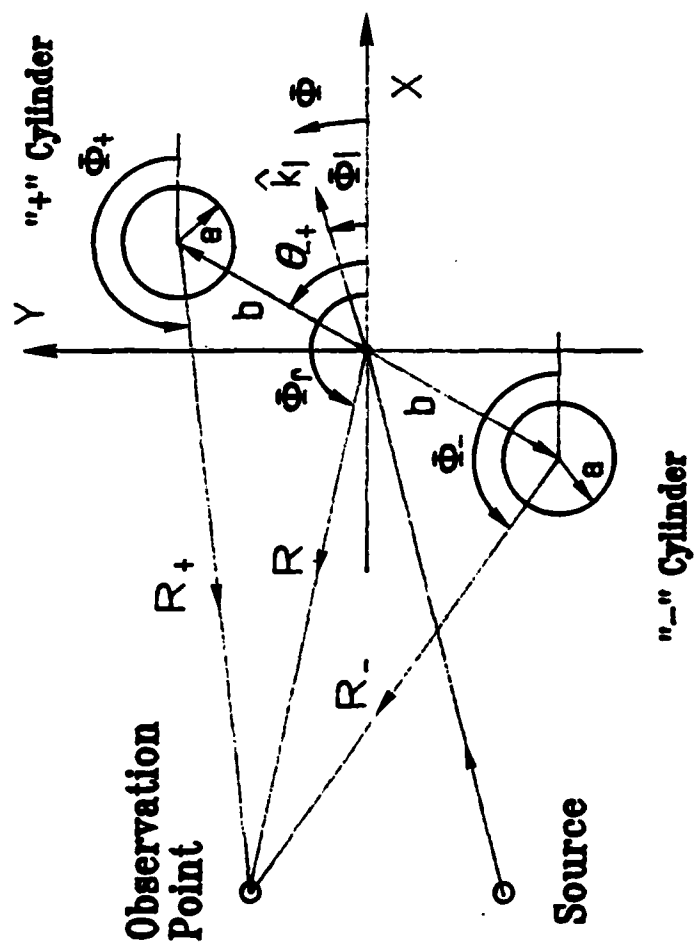
[15] V. Twersky, "Mutiple Scattering of Radiation by an Arbitrary Configuration of Parallel Cylinders", The Journal of the Acoustical Society of America, Vol.24, No.1, Jan. 1952, pp.42-46

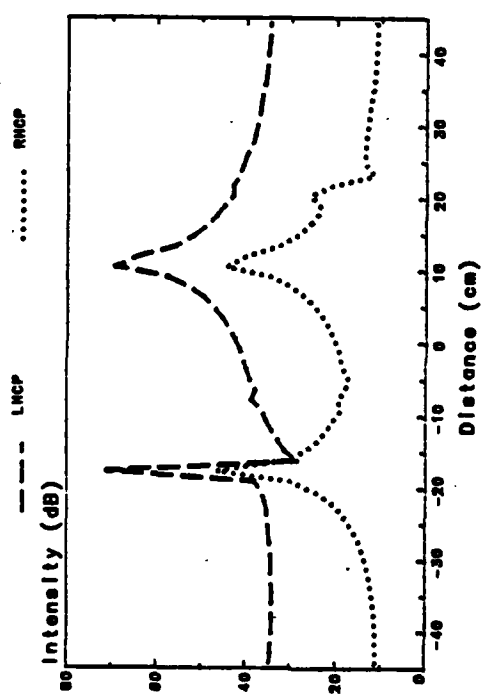
LIST OF FIGURES

- Fig. 1. Scattering geometry of a single infinitely long cylinder.
- Fig. 2. Magnitudes (a) and phases (b) of the LHCP and RHCP components of the directly scattered field from a single cylinder of radius $a=3.8$ cm illuminated by a RHCP plane wave obtained for a range $4.79 < ka < 13.57$ and (c) reconstructed range profiles.
- Fig. 3. Scattering geometry of two parallel infinitely long cylinders.
- Fig. 4. Reconstructed range profiles of the LHCP and RHCP directly scattered fields of two cylinders.
- Fig. 5. Polar plots of (a) LHCP and (b) RHCP directly scattered fields of two cylinders.
- Fig. 6. Results of reconstructed images of two cylinders from (a) LHCP and (b) RHCP directly scattered fields data.
- Fig. 7. Magnitude (a) and phase (b) of the RHCP and LHCP mutually scattered fields of two cylinders, and (c) reconstructed range profiles for $\phi_i = 6^\circ$.
- Fig. 8. Polar plots of (a) RHCP and (b) LHCP mutually scattered fields of two cylinders.
- Fig. 9. Reconstructed images of two cylinders from numerically generated (a) RHCP and (b) LHCP mutually scattered field data for $\phi_i = 6^\circ$, and from RHCP data for (c) $\phi_i = 8^\circ$ and (d) $\phi_i = 0^\circ$.
- Fig. 10. Polar representations of (a) RHCP and (b) LHCP scattering data of two cylinders and associated images obtained by Fourier inversion.
- Fig. 11. Measurement system situated in an anechoic chamber environment.
- Fig. 12. Experimentally obtained polar representations of (a) RHCP and (b) LHCP scattering data and associated images obtained by Fourier inversion.

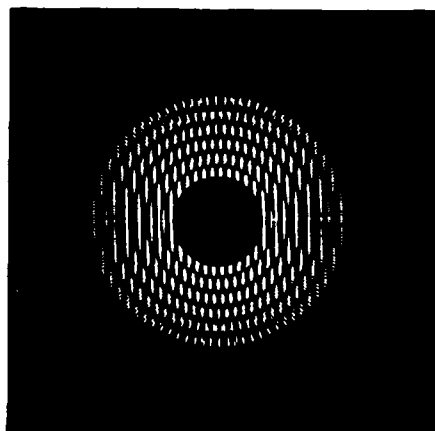




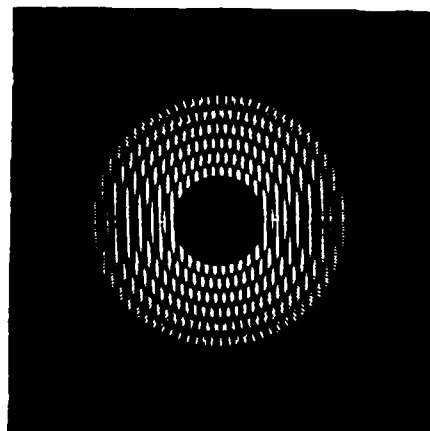




Top

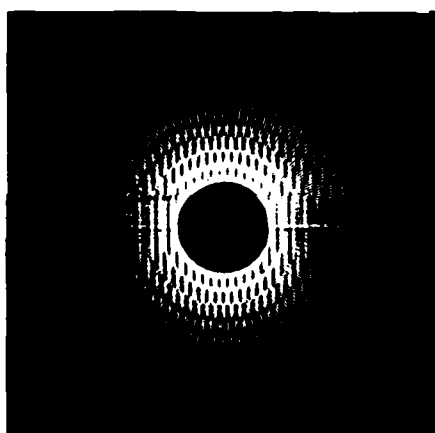


Real part

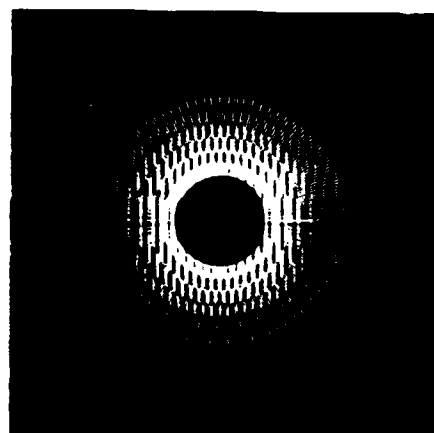


Imaginary part

(a)

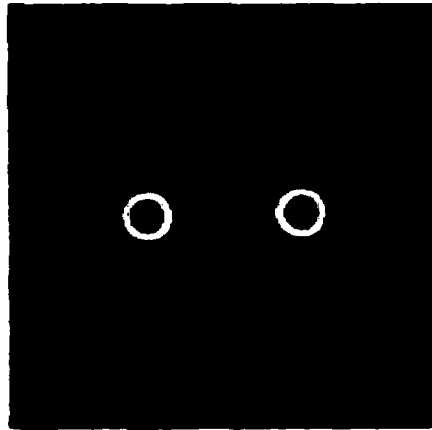


Real part



Imaginary part

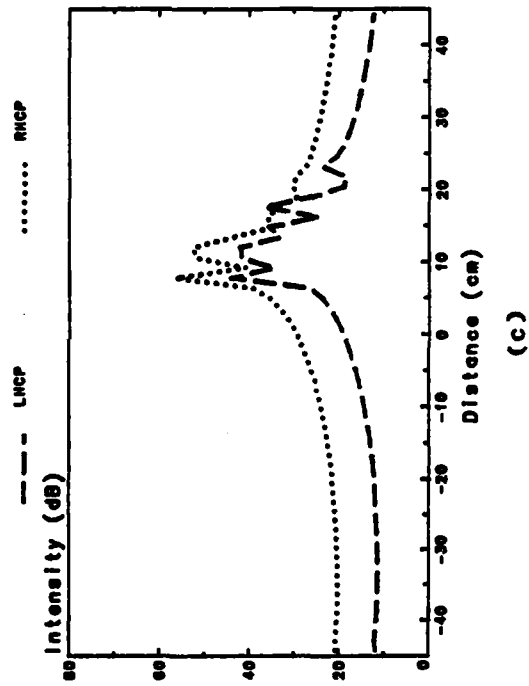
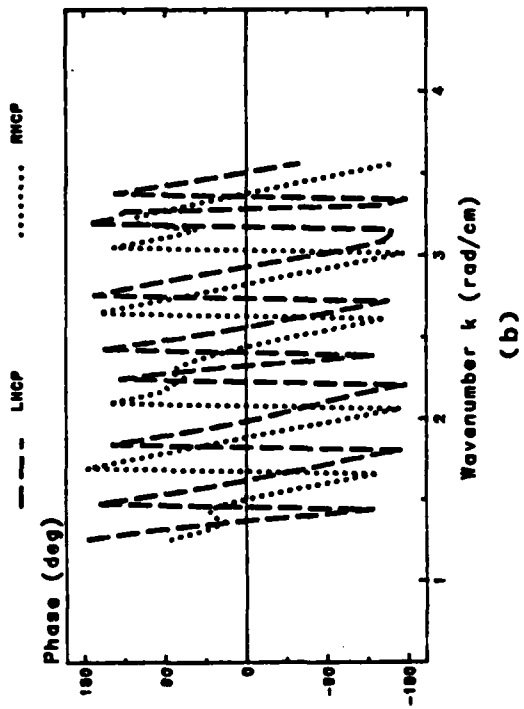
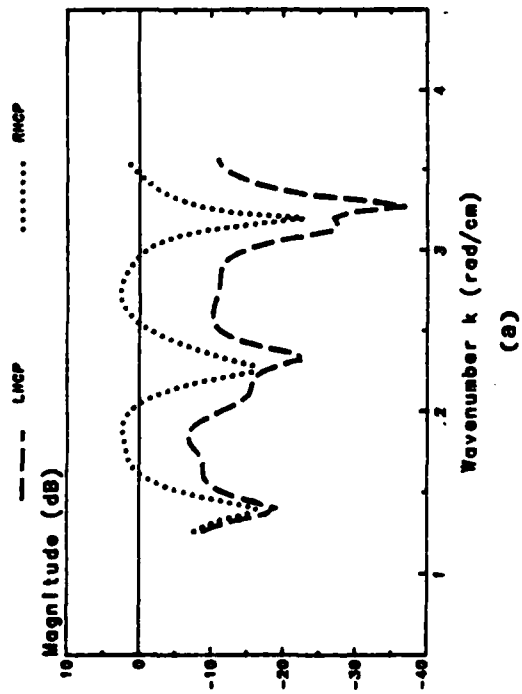
(b)

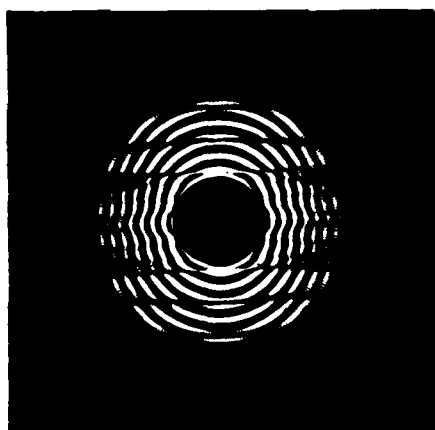


(a)

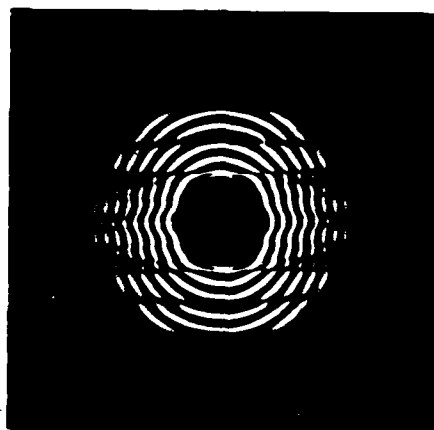


(b)



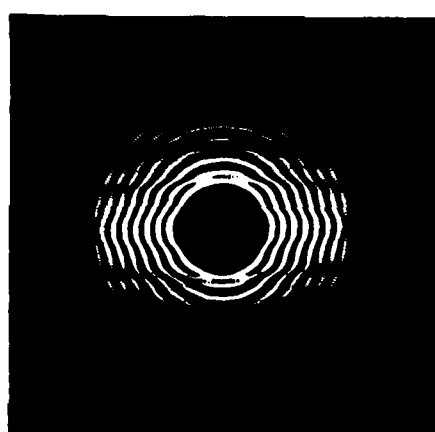


Real part

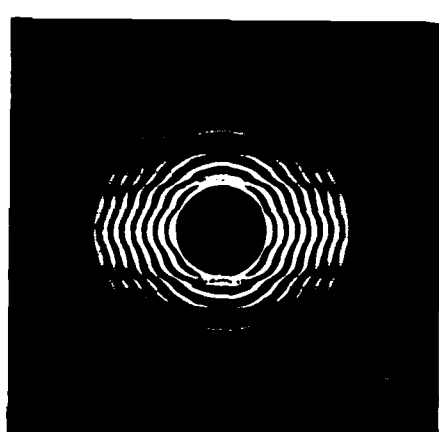


Imaginary part

(a)

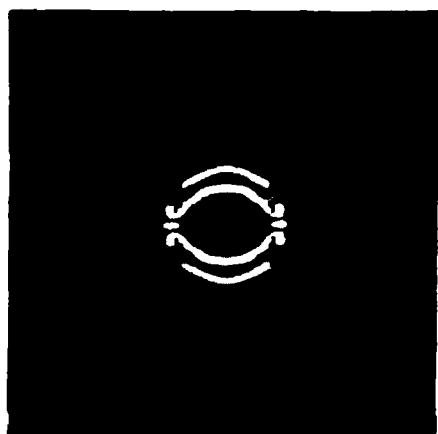


Real part

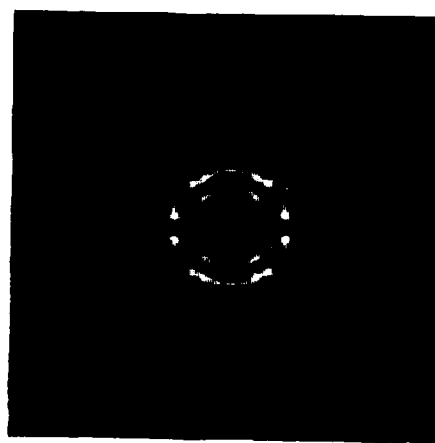


Imaginary part

(b)



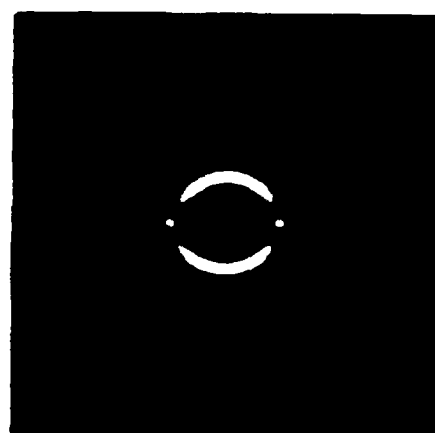
(a)



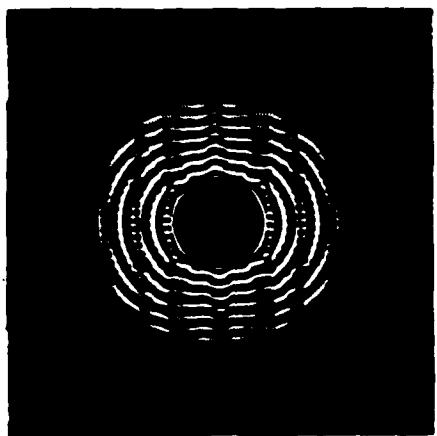
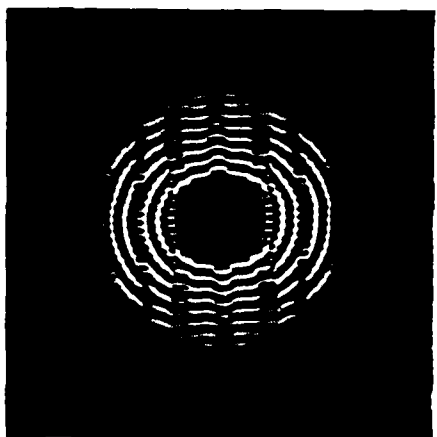
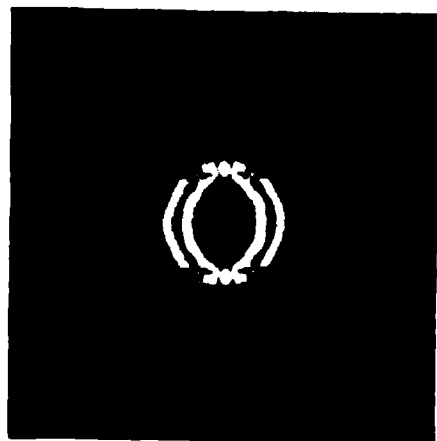
(b)



(c)

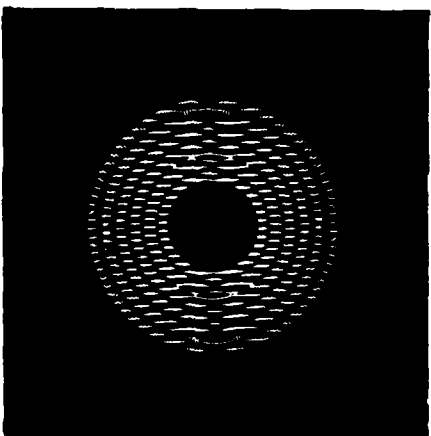
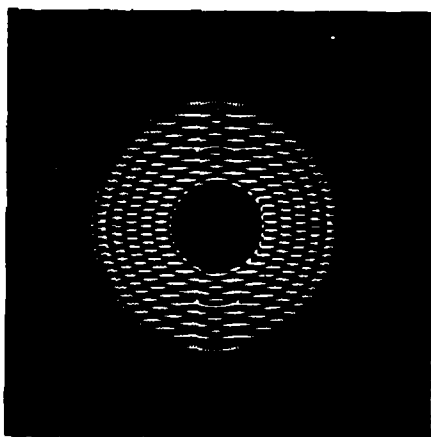
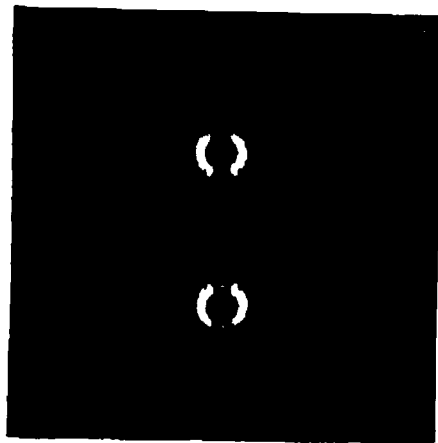


(d)



Imaginary part

(a)

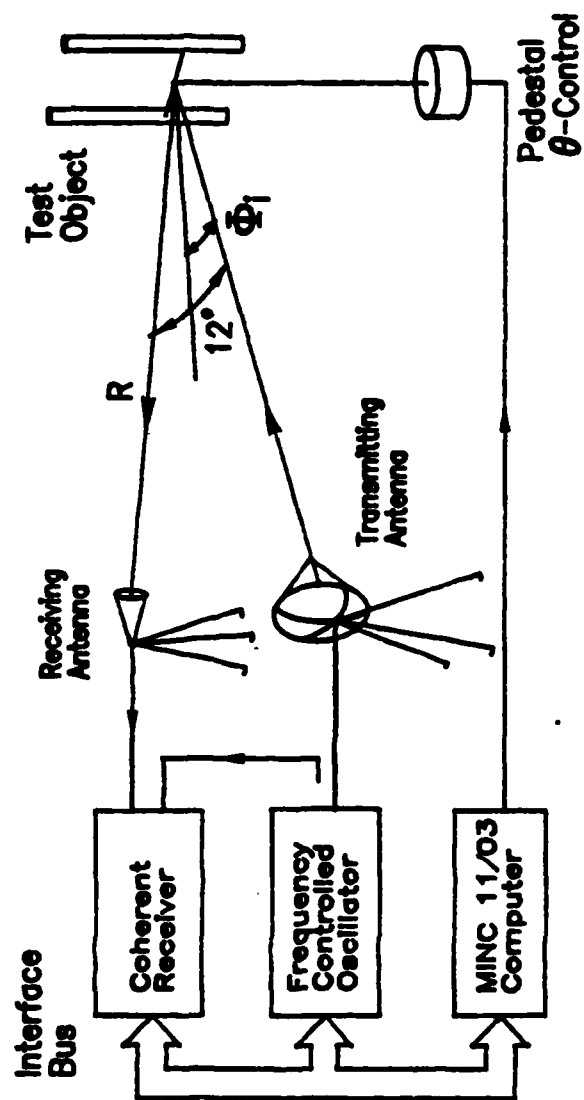


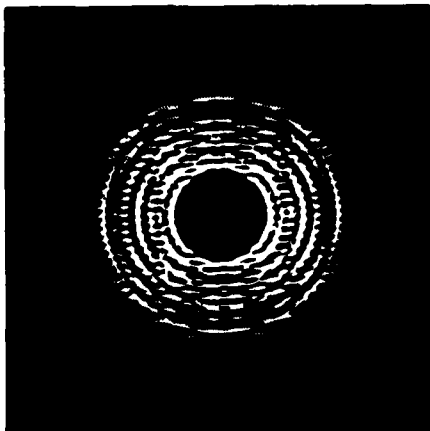
Imaginary part

(b)

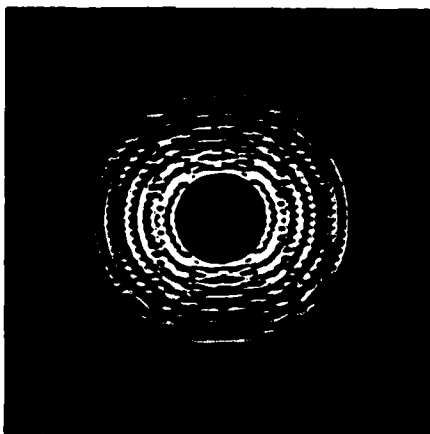
Real part

Real part



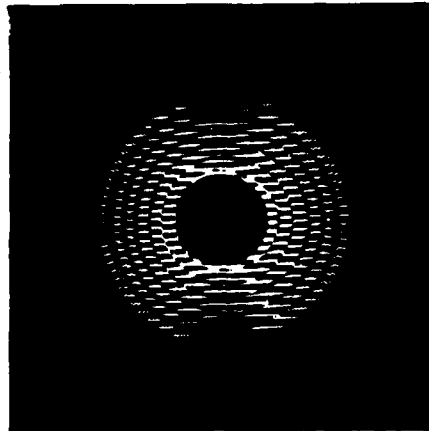
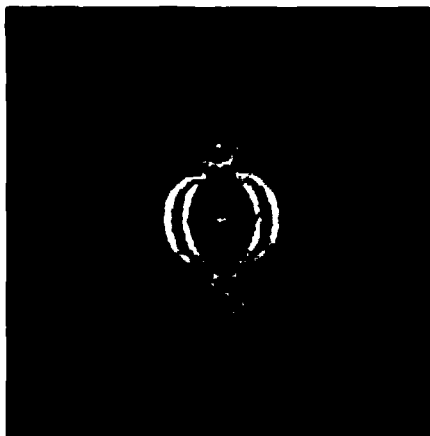


Real part

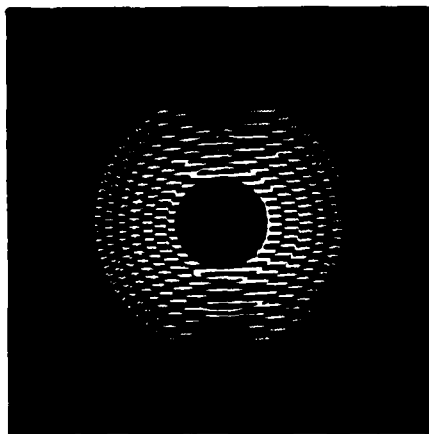


Imaginary part

(a)

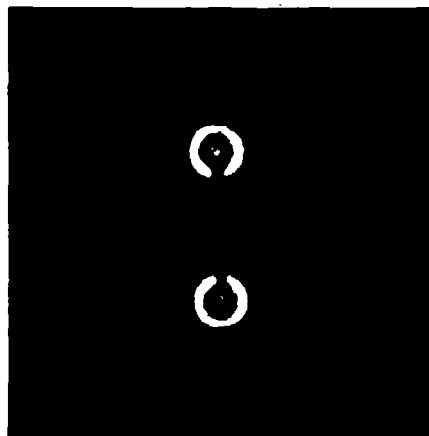


Real part



Imaginary part

(b)



APPENDIX II

MICROWAVE DIVERSITY IMAGING OF OBJECTS IN THE PRESENCE OF SEVERE CLUTTER

Nabil H. Farhat and Yuhsyen Shen

University of Pennsylvania
The Moore School of Electrical Engineering
Electro-Optics and Microwave-Optics Laboratory
Philadelphia, PA 19104

ABSTRACT

Microwave diversity imaging techniques in which spectral angular (aspect dependent) and polarization degrees of freedom are employed in image formation are shown to be effective in high resolution projection imaging of targets in the presence of severe clutter. Principles, methodologies, and experimental results demonstrating this capability are presented. Implications of the results for air-borne or space-borne down looking imaging radars and imaging of internal structure of penetrable objects are also discussed.

I. INTRODUCTION

Frequently microwave imaging situations arise where the object being imaged is situated against a strongly reflecting background that produces severe clutter or is obstructed by clutter producing surfaces or foreground. Examples are found in air-borne or space-borne down-looking imaging radars and systems for the imaging of internal structure of penetrable bodies. The aim of this paper is to demonstrate the capability of a high resolution microwave diversity imaging system in discriminating objects of interest in the presence of such severe clutter. The approach is based on a *spot-light imaging mode* in which spectral, angular, and polarization diversities are utilized to access the three-dimensional Fourier space of a coherently illuminated microwave scene. A brief theoretical review of the principle is presented followed by a description of the microwave imaging configuration employed in collecting realistic data of a representative situation: that of a low flying aircraft. The antennas in the imaging configurations studied are positioned as if they were space-borne looking downward towards the target and the ground. Only one two-dimensional slice of the three-dimensional Fourier space is obtained; hence the reconstructed image is a projective side-view. The reconstructed images show clearly the ability to distinguish the object image from the background clutter simulated in our experiments by ground planes overlayed by crumbled aluminum foil. The

polarization-enhanced microwave images obtained are comparable visually to high contrast side-view photographs of the scene taken with flood light illumination. Finally the effect of relative motion and how to account for it in the measurement is discussed. The results shown demonstrate clearly the ability to form recognizable high resolution images of complex scatterers in the presence of severe clutter.

II. THEORETICAL BACKGROUND

It has been demonstrated that by combining angular, spectral, and polarization diversities in a coherent imaging system, projective or tomographic images of complex shaped conducting bodies can be obtained with near optical resolution [1]. The principles on which such a system is based are obtained from inverse scattering theory [2,3,4], which shows that under the physical optics and Born approximations, the scalar component associated with one polarization of the fields scattered in the direction of the unit vector \hat{l}_R and observed at a distance R from an object illuminated by a plane wave incident in the direction of the unit vector \hat{l}_I is given by [5]

$$\psi(\vec{p}, R) = \frac{jAk}{2R} e^{-jkR} \int_{-\infty}^{\infty} \gamma(\vec{r}) e^{j\vec{p} \cdot \vec{r}} d\vec{r} \quad (1)$$

where $\gamma(\vec{r})$ is the object scattering function which is a function of positional vector \vec{r} referred to an arbitrarily chosen reference origin in the object. $\gamma(\vec{r})$ represents the 3-D distribution of scattering centers on the target, assumed to be non-dispersive, i.e., γ is independent of frequency ω , and as such is closely related to the surface contour of the object. The vector $\vec{p} = k(\hat{l}_R - \hat{l}_I)$, is the positional vector in the Fourier space. In particular, $\vec{p} = 2k\hat{l}_R$ in the monostatic case, i.e., when transmitter and receiver (T/R) antennas are closely positioned. $k = \omega/c$ is the wavenumber, c being the velocity of light.

By correcting for the range-related term in front of the integral in eq. (1), we obtain a three-dimensional Fourier transform relationship between the corrected data and the object scattering function,

$$\Gamma(\bar{p}) = \int_{-\infty}^{\infty} \gamma(\bar{r}) e^{j\bar{p} \cdot \bar{r}} d\bar{r} = -j \frac{2\pi R}{Ak} e^{jkR} \psi(\bar{p}, R) \quad (2)$$

This permits the retrieval of $\gamma(\bar{r})$ by Fourier inversion of the measured data ψ corrected for the range dependent factor preceding the integral in eq. (1). Techniques for determining R with sufficient accuracy to perform the range correction and for correcting for the frequency response of the measurement system were described elsewhere [1]. Note that the \bar{p} -space data, or $\Gamma(\bar{p})$, can be acquired over different values of \bar{p} by varying \hat{l}_R , \hat{l}_1 , and k . *Angular diversity*, or angular degrees of freedom involve changing \hat{l}_R and/or \hat{l}_1 while varying k involves spectral degrees of freedom and is referred to as *spectral diversity*. The object scattering function depends generally on polarization, which allows us to exploit *polarization diversity* to further enrich the accessed volume of the Fourier space with polarization related information about the object. Even though physical optics considerations predict no depolarization in monostatic scattering measurements some depolarization exists in practice. (Depolarization effects become markedly noticeable for the bi-static case). In the experiments described below the co-polarized and cross-polarized components of the scattered field are measured for different status polarization of the incident illumination and the image intensities formed from them are added to obtain a polarization enhanced image. A more detailed discussion of the role of polarization in microwave diversity imaging will be given elsewhere [5].

The reconstructed image quality depends on the size of the \bar{p} -space accessed by measurement. The size of \bar{p} -space depends on the values of \bar{p}

realized in the measurements as imposed by the spectral and angular windows realized by the measurement gear. In order to avoid aliasing of the retrieved image care must be taken to choose the values of \bar{p} so as to satisfy the Nyquist criterion.

The inherently two-dimensional nature of most image display devices leads to two types of two-dimensional presentation that are of prime interest. One is *tomographic*, or cross-sectional, presentation of a three-dimensional object. Given the acquired $\Gamma(\bar{p})$ data in three-dimensional \bar{p} -space, one may use the *weighted projection-slice theorem* [6], which is the generalization of the well-known *projection-slice theorem* [7], to reconstruct and display a specific tomogram of the three-dimensional object. The other presentation is a *projective image* of the three-dimensional body. From the projection-slice theorem, the projective image can be reconstructed from a central slice, or meridional slice of \bar{p} -space data. The imaging geometry to be described in the next section accesses one such meridional slice, hence the retrieved images presented here are projective.

III. SIMULATION GEOMETRY AND EXPERIMENT

Figure 1 depicts the situation to be simulated, in which a space-borne imaging platform containing a coherent broad-band T/R system is looking downward toward an aircraft flying at low altitude. The imaging platform tracks the aircraft in a *spot-light* fashion. For simplicity, we assume that the platform moves relatively much faster than the aircraft, and that during the period in which the platform acquires data for one aspect look of the aircraft, the change in aircraft is negligible. In actual situations, this assumption is not valid. Doppler shift caused by the variation of distance between the platform and the aircraft during the data acquisition period of

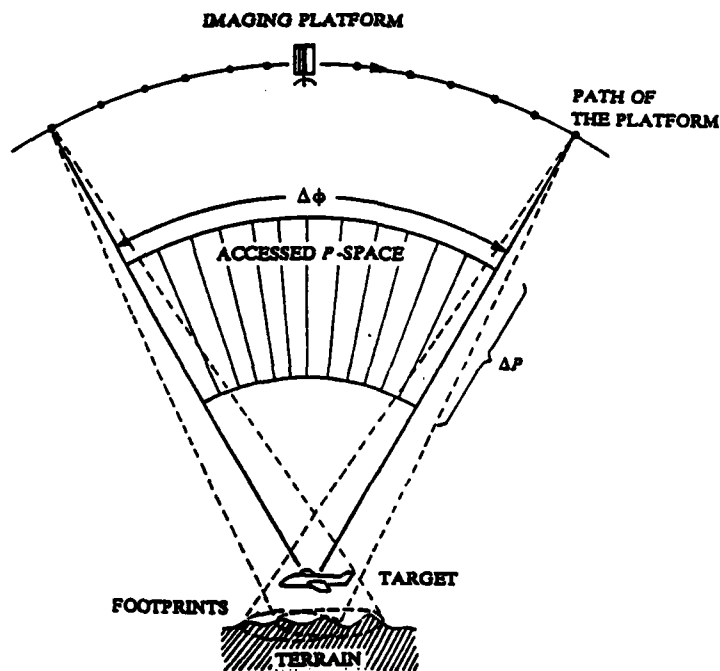


Fig. 1. Simulated imaging geometry.

one look complicates the data acquisition as well as data processing. What we simulate here is an ideal case which removes the unwanted complexity to show what can ultimately be achieved with an imaging system that can account for the doppler shift and hence can access the 3-D Fourier space of target in the presence of relative motion. Also shown in Fig. 1 is the \bar{p} -space data accessed, where $\Delta p = 2\Delta k = 2\Delta\omega/c$, is proportional to the spectral window $\Delta\omega/2\pi$ utilized. Note that the data lie on a polar grid. It represents a meridional slice of the three-dimensional \bar{p} -space or Fourier space of the object. Thus the retrieved images will be projective, with projection direction perpendicular to the plane of the \bar{p} -space slice.

To simulate strong ground clutter, a light cardboard plate covered with a layer of crumbled aluminum foil is employed as a roughened ground plate or background. Two such plates are used; one with rms height variation greater than the mean wavelength of the spectral window employed, the other with rms

height variations less than the mean wavelength. The clutter plate is mounted on a styrofoam support with a 75:1 metalized scale model of the space shuttle placed in front of the plate at a distance representing altitude as depicted in Fig. 2. The transmitting/receiving (T/R) antennas are oriented as if they were looking downward towards the target. A small bistatic angle $\alpha \approx 15.6^\circ$ between the T/R antennas, is used to allow insertion of an absorbing isolating screen to minimize coupling between them. Thus the scattering geometry is not strictly monostatic and the effect of finite α can be seen from $\bar{p} = k (\hat{l}_R - \hat{l}_I) = 2k \cos \frac{\alpha}{2} \hat{l}_p$ where \hat{l}_p is a unit vector in the \bar{p} direction bisecting α and α is the bistatic angle. The effective frequency is therefore the actual frequency multiplied by $\cos(\alpha/2)$.

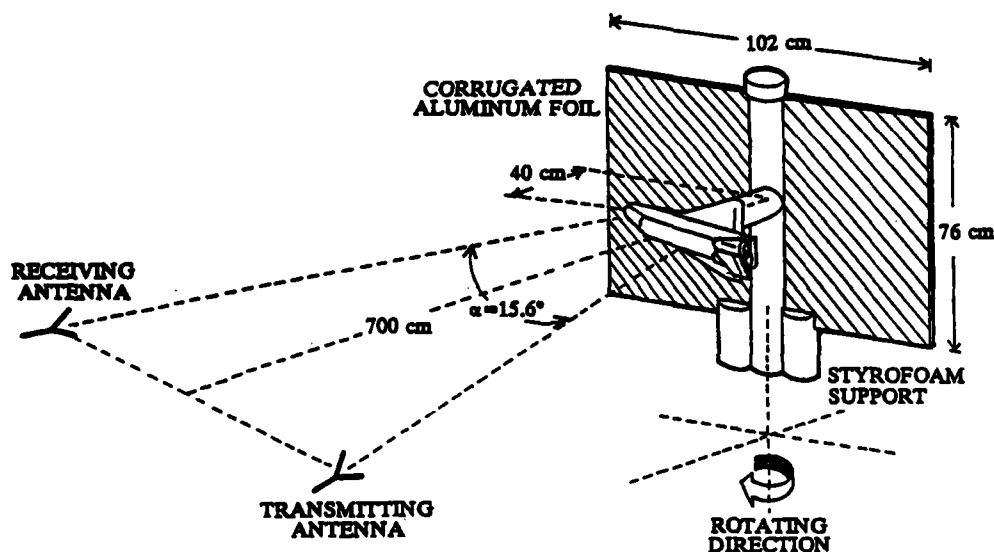


Fig. 2. Experimental imaging arrangement.

High resolution can be achieved through the use of wide spectral and angular windows. In principle narrow impulsive illumination with wide spectral content can be used to achieve good range resolution, but usually is difficult to implement with sufficient power. Dispersed pulses together with post-detection com-

pression may provide both the power and spectral window width needed. But this approach can be restricted by the detector bandwidth, which is typically a fraction of the central frequency. The availability of computer-tunable wide band RF sources, e.g., sweep oscillators and synthesizers, makes it feasible to generate effectively an extremely narrow pulse using frequency synthesis. This indirect pulse synthesis is the approach we take to achieve high resolution. Typically a spectral window of $\Delta f \approx 11$ GHz covering a frequency range from 6.1 to 17.5 GHz is used. The number of frequency increments used to cover this spectral range was 128. This provides a range resolution $\delta R = c/2\Delta f$ of better than 1.5 cm. The angular window $\Delta\phi$, seen in Fig. 1, used in acquiring data in the results presented below covered 90 degrees. The number of angular samples or looks in each window is 128.

Data for four possible combinations of circular polarization states of the T/R antennas are collected. These are designated in accordance to the receiver and transmitter polarizations following the nomenclature used in [8]. For example, RL represents the data collected by a right hand circularly polarized (RHCP) receiving antenna when the object is illuminated by a left hand circularly polarized (LHCP) plane wave produced by a LHCP transmitting antenna. When the T/R antennas are of opposite polarization states, we call the measurement co-polarized, because of the phase reversal of the incident wave upon reflection from a metalized object. On the other hand, and for the same reason, cross-polarization applies to measurement when the T/R antennas have identical polarization states. Polarization enhanced images are obtained by incoherent combination of the images retrieved from co- and cross-polarized Fourier space data.

IV. EXPERIMENTAL RESULTS

Techniques for minimizing anechoic chamber clutter and for correcting the data for the measurement system response and for the range-related term in eq. (1) are described in details in [1]. After the correction, the \bar{p} -space data, which is obtained in polar format, are interpolated onto a Cartesian grid to facilitate image retrieval by Fourier inversion using the fast Fourier transform (FFT) algorithm. A four nearest neighbors interpolation [6] is used. The real (top) and imaginary (bottom) parts are shown on the left together with the reconstructed image on the right. The data and the image shown are of the space shuttle alone without the clutter plate in position when the receiver is LHCP and the transmitter is RHCP i.e., a co-polarized image, hence the designation LR in the caption of this figure.



Fig. 3. Interpolated \bar{p} -space data (left) and image (right) of the space shuttle. Co-polarized or LR case (R-LHCP, T-RHCP).

The \bar{p} -space data and the image of the same polarization states when the rougher clutter plate was placed as background behind the shuttle are shown in Fig. 4. We note that the fringes in the \bar{p} -space data are dominated now by those produced by the clutter plate, and that only at central aspect looks one can distinguish fringe structure due to the shuttle.



Fig. 4. \bar{P} -space data (left) and image (right) of the shuttle above the rougher ground plate. Co-polarized or LR case. (R-LHCP, T-RHCP).

Figure 5 shows the results obtained with the same conditions of Fig. 4 except that the polarization state is now RR. It can be seen that the image of the clutter plate is seen to be similar to the LR case, but the image of the specularly reflecting shuttle model is somewhat different containing some complementary information.



Fig. 5. \bar{P} -space data (left) and image (right) of the shuttle above the rougher ground plate. Cross-polarized case (R-RHCP, T-RHCP).

The polarization enhanced image, the result of adding the image intensities of Figs. 4 and 5, is shown in Fig. 6 together with a high contrast pictorial side view of the space shuttle on its mount shown for comparison taken under flood-light conditions to emphasize similar outline. The similarity of the two images is striking. Most of the features of the shuttle are present without much degradation by the influence of the clutter plate. This is attributed primarily to the wide dynamic range of the measurement system estimated to be 68 dB, which enables the delineation of weak scattering detail in the presence of strong scatterers, and due to the excellent range resolution (~1.5 cm) which enables isolating the clutter image spatially.

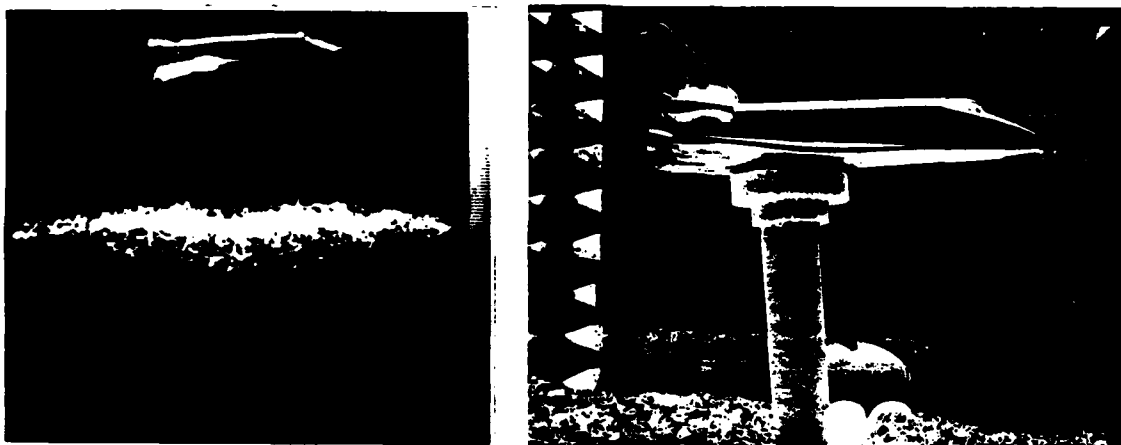


Fig. 6. Polarization enhanced image (RR+LR) (left) and optical image (right).

Enhanced images of the shuttle with each of the two clutter plates (of different rms height variations) are shown in Fig. 7. The image with the smoother clutter plate compares less favorably to that with rougher clutter plate. The shuttle is less visible and artifact is present in the clutter image. The weaker shuttle image is believed to be due to the less diffuse nature of scattering from the smoother plate which tends to produce stronger

backscatter signals than from the rougher plate. One conjecture for the artifact is the multiple reflection between the shuttle, styrofoam support, and the plate. Notice also the appearance of a weak "reflection" image of the shuttle in the smoother clutter plate.

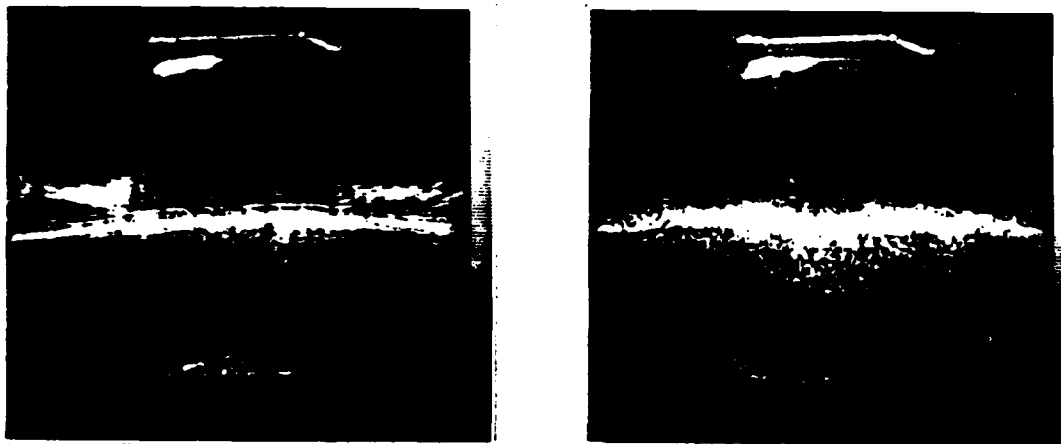


Fig. 7. Polarization enhanced images of the shuttle with different plates. (left: rms height < mean wavelength; right: rms height > mean wavelength.)

V. DISCUSSIONS AND CONCLUSIONS

We have demonstrated for the first time that despite the presence of the relatively strong background clutter, images of high quality can be obtained with a high resolution system. The microwave images are comparable visually to their visual counterparts under mono-directional floodlight illumination. Although for the images shown here a 90 degree angular window is utilized, reduction of the window size down to 30 degrees continued to yield discernible, though somewhat degraded, images of the target.

Separation of the target from the clutter may be desirable. Spatial filtering in the image plane can be employed to achieve this. Coherent subtraction in the \bar{p} -space is another way in which the \bar{p} -space data of the

ground plate alone is subtracted from the \bar{p} -space data of the shuttle plus the ground plate. We find that this latter approach is not easy to implement with our present set-up because of the difficulty of duplicating the exact aspect looks at different runs of experiments. Slight change of the object aspect may not change the magnitude of the \bar{p} -space data, but the phase can be altered noticeably, which makes the coherent removal of the clutter difficult. In actual situations, this strategy is impractical since it requires measurement of the same clutter at exactly the same aspect looks twice; once when the target is present, the other without. The more feasible practice as stated earlier is separating the clutter in the image space by spatial filtering. The one-dimensional FFT of the data at each look is the range profile of the scene at that aspect look. With good range resolution, detail belonging to the image of the object and that of the clutter can be separated.

As mentioned earlier, the simulated conditions in the above study are ideal, i.e., the target motion is ignored. In actuality, the imaging platform and the target are in relative motion. It is however the change of aspect of the object scene during motion that provides image formation; i.e., it is the changes of their relative orientations that contributes to image formation. This has been the central process in the spot-light imaging scheme studied here. The effect of relative motion is merely to introduce doppler shift in the frequency of the received echo. Compensating for the doppler shift in the measurement methodology described here would allow accessing the \bar{p} -space of a moving target in the manner described above. Methods for removing the doppler shift caused by relative motion are currently under study. One promising method being studied utilizes what we call "orchestrated frequency response measurement" in which the doppler shift of the echo relative to the

transmitted signal is rapidly determined and the information used to set the frequency of a synthesized source used as local oscillator for the receiver to a value needed to compensate for doppler shift. The L.O. synthesizer in this scheme is phase-locked to a transmitter synthesizer providing the object illumination. Equipment for performing this study obtained under a \$350K DoD/URIP grant is presently being assembled. The result of this study will be reported on in the near future.

VI. ACKNOWLEDGEMENT

The work reported here was supported by a grant from General Electric Co. and under partial support from the Air Force Office of Scientific Research.

VII. REFERENCES

1. N.H. Farhat, et. al., "Prospects for Three-dimensional Projective and Tomographic Imaging Radar Networks," Radio Science, Vol. 19, No. 5, pp. 1347-1355, Sept.-Oct. 1984. (see also Appendix I of this document)
2. R.M. Lewis, "Physical Optics Inverse Diffraction," IEEE Trans. on Antennas & Propagations, Vol. AP-17, pp. 308-314, 1969.
3. N. Bojarski, "Inverse Scattering," Final Report N000 19-73-C-0312F, Nav. Air Syst. Command, Warminster, PA., February 1974.
4. S.R. Raz, "On Scatterer Reconstruction from Far-field Data," IEEE Trans. on Antennas & Propagations, Vol. AP-24, pp. 66-70, 1976.
5. T.H. Chu and N.H. Farhat, "Polarization Effects in Microwave Diversity Imaging of Conducting Cylinders," submitted for publication.
6. C.K. Chan and N.H. Farhat, "Frequency Swept Tomographic Imaging of Three-Dimensional Perfectly Conducting Objects," IEEE Trans. on Antennas & Propagations, Vol. AP-29, pp. 321-319, 1981.
7. R.M. Mersereau and A.V. Oppenheim, "Digital Reconstruction of Multidimensional Signals from Their Projections," Proc. IEEE, Vol. 62, pp. 1319-1338, 1978.
8. G.T. Ruck, et. al., Chapter 2 in Radar Cross Section Handbook, Vol. 1, G.T. Ruck (Ed.), Plenum Press, New York, 1970.

Reprinted from *Applied Optics*, Vol. 24, page 1469, May 15, 1985
 Copyright © 1985 by the Optical Society of America and reprinted by permission of the copyright owner.

Optical implementation of the Hopfield model

Nabil H. Farhat, Demetri Psaltis, Aluizio Prata, and Eung Paek

Optical implementation of content addressable associative memory based on the Hopfield model for neural networks and on the addition of nonlinear iterative feedback to a vector-matrix multiplier is described. Numerical and experimental results presented show that the approach is capable of introducing accuracy and robustness to optical processing while maintaining the traditional advantages of optics, namely, parallelism and massive interconnection capability. Moreover a potentially useful link between neural processing and optics that can be of interest in pattern recognition and machine vision is established.

I. Introduction

It is well known that neural networks in the eye-brain system process information in parallel with the aid of large numbers of simple interconnected processing elements, the neurons. It is also known that the system is very adept at recognition and recall from partial information and has remarkable error correction capabilities.

Recently Hopfield described a simple model¹ for the operation of neural networks. The action of individual neurons is modeled as a thresholding operation and information is stored in the interconnections among the neurons. Computation is performed by setting the state (on or off) of some of the neurons according to an external stimulus and, with the interconnections set according to the recipe that Hopfield prescribed, the state of all neurons that are interconnected to those that are externally stimulated spontaneously converges to the stored pattern that is most similar to the external input. The basic operation performed is a nearest-neighbor search, a fundamental operation for pattern recognition, associative memory, and error correction. A remarkable property of the model is that powerful global computation is performed with very simple, identical logic elements (the neurons). The interconnections provide the computation power to these simple logic elements and also enhance dramatically the stor-

age capacity; approximately $N/4 \ln N$ bits/neuron can be stored in a network in which each neuron is connected to N others.² Another important feature is that synchronization among the parallel computing elements is not required, making concurrent, distributed processing feasible in a massively parallel structure. Finally, the model is insensitive to local imperfections such as variations in the threshold level of individual neurons or the weights of the interconnections.

Given these characteristics we were motivated to investigate the feasibility of implementing optical information processing and storage systems that are based on this and other similar models of associative memory.^{3,4} Optical techniques offer an effective means for the implementation of programmable global interconnections of very large numbers of identical parallel logic elements. In addition, emerging optical technologies such as 2-D spatial light modulators, optical bistability, and thin-film optical amplifiers appear to be very well suited for performing the thresholding operation that is necessary for the implementation of the model.

The principle of the Hopfield model and its implications in optical information processing have been discussed earlier.^{5,6} Here we review briefly the main features of the model, give as an example the results of a numerical simulation, describe schemes for its optical implementation, then present experimental results obtained with one of the schemes and discuss their implications as a content addressable associative memory (CAM).

II. Hopfield Model

Given a set of M bipolar, binary (1, -1) vectors $\mathbf{v}_i^{(m)}$, $i = 1, 2, 3 \dots N$, $m = 1, 2, 3 \dots M$, these are stored in a synaptic matrix in accordance with the recipe

$$T_{ij} = \sum_{m=1}^M v_i^{(m)} v_j^{(m)}, \quad i, j = 1, 2, 3 \dots N, \quad T_{ii} = 0, \quad (1)$$

$\mathbf{v}_i^{(m)}$ are referred to as the nominal state vectors of the

Nabil Farhat is with University of Pennsylvania, Moore School of Electrical Engineering, Philadelphia, Pennsylvania 19104; the other authors are with California Institute of Technology, Electrical Engineering Department, Pasadena, California 91125.

Received 24 December 1984.

0003-6835/85/101469-07\$02.00/0.

© 1985 Optical Society of America.

memory. If the memory is addressed by multiplying the matrix T_{ij} with one of the state vectors, say $v_i^{(mo)}$, it yields the estimate

$$\hat{\phi}_i^{(mo)} = \sum_j T_{ij} v_j^{(mo)} \quad (2)$$

$$\begin{aligned} &= \sum_{j=1}^N \sum_{m=1}^M v_i^{(m)} v_j^{(m)} v_j^{(mo)} \\ &= (N-1)v_i^{(mo)} + \sum_{m \neq mo} \alpha_{m,mo} v_i^{(m)}, \end{aligned} \quad (3)$$

where

$$\alpha_{m,mo} = \sum_j v_j^{(mo)} v_j^{(m)}.$$

$\hat{\phi}_i^{(mo)}$ consists of the sum of two terms: the first is the input vector amplified by $(N-1)$; the second is a linear combination of the remaining stored vectors and it represents an unwanted cross-talk term. The value of the coefficients $\alpha_{m,mo}$ is equal to $\sqrt{N-1}$ on the average (the standard deviation of the sum of $N-1$ random bits), and since $(M-1)$ such coefficients are randomly added, the value of the second term will on the average be equal to $\sqrt{(M-1)(N-1)}$. If N is sufficiently larger than M , with high probability the elements of the vector $\hat{\phi}_i^{(mo)}$ will be positive if the corresponding elements of $v_i^{(mo)}$ are equal to +1 and negative otherwise. Thresholding of $\hat{\phi}_i^{(mo)}$ will therefore yield $v_i^{(mo)}$:

$$v_i^{(mo)} = \text{sgn}[\hat{\phi}_i^{(mo)}] = \begin{cases} +1 & \text{if } \hat{\phi}_i^{(mo)} > 0 \\ -1 & \text{otherwise.} \end{cases} \quad (4)$$

When the memory is addressed with a binary valued vector that is not one of the stored words, the vector-matrix multiplication and thresholding operation yield an output binary valued vector which, in general, is an approximation of the stored word that is at the shortest Hamming distance from the input vector. If this output vector is fed back and used as the input to the memory, the new output is generally a more accurate version of the stored word and continued iteration converges to the correct vector.

The insertion and readout of memories described above are depicted schematically in Fig. 1. Note that in Fig. 1(b) the estimate $\hat{\phi}_i^{(mo)}$ can be viewed as the weighted projection of T_{ij} . Recognition of an input vector that corresponds to one of the state vectors of the memory or is close to it (in the Hamming sense) is manifested by a stable state of the system. In practice unipolar binary (0,1) vectors or words $b_i^{(m)}$ of bit length N may be of interest. The above equations are then applicable with $[2b_i^{(m)} - 1]$ replacing $v_i^{(m)}$ in Eq. (1) and $b_i^{(mo)}$ replacing $v_i^{(mo)}$ in Eq. (2). For such vectors the SNR of the estimate $\hat{\phi}_i^{(mo)}$ can be shown to be lower by a factor of $\sqrt{2}$.¹

An example of the T_{ij} matrix formed from four binary unipolar vectors, each being $N = 20$ bits long, is given in Fig. 2 along with the result of a numerical simulation of the process of initializing the memory matrix with a partial version of $b_i^{(4)}$ in which the first eight digits of $b_i^{(4)}$ are retained and the remainder set to zero. The Hamming distance between the initializing vector and $b_i^{(4)}$ is 6 bits and it is 9 or more bits for the other three

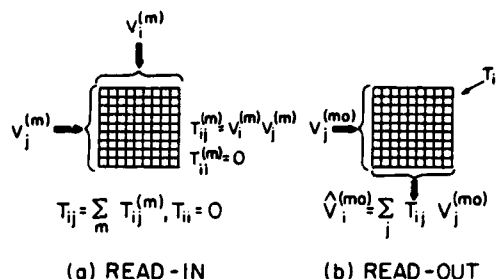


Fig. 1. (a) Insertion and (b) readout of memories.

stored vectors. It is seen that the partial input is recognized as $b_i^{(4)}$ in the third iteration and the output remains stable as $b_i^{(4)}$ thereafter. This convergence to a stable state generally persists even when the T_{ij} matrix is binarized or clipped by replacing negative elements by minus ones and positive elements by plus ones evidencing the robustness of the CAM. A binary synaptic matrix has the practical advantage of being more readily implementable with fast programmable spatial light modulators (SLM) with storage capability such as the Litton Lightmod.⁷ Such a binary matrix, implemented photographically, is utilized in the optical implementation described in Sec. III and evaluated in Sec. IV of this paper.

Several schemes for optical implementation of a CAM based on the Hopfield model have been described earlier.⁵ In one of the implementations an array of light emitting diodes (LEDs) is used to represent the logic elements or neurons of the network. Their state (on or off) can represent unipolar binary vectors such as the state vectors $b_i^{(m)}$ that are stored in the memory matrix T_{ij} . Global interconnection of the elements is realized as shown in Fig. 3(a) through the addition of nonlinear feedback (thresholding, gain, and feedback) to a conventional optical vector-matrix multiplier⁸ in which the array of LEDs represents the input vector and an array of photodiodes (PDs) is used to detect the output vector. The output is thresholded and fed back in parallel to drive the corresponding elements of the LED array. Multiplication of the input vector by the T_{ij} matrix is achieved by horizontal imaging and vertical smearing of the input vector that is displayed by the LEDs on the plane of the T_{ij} mask [by means of an anamorphic lens system omitted from Fig. 3(a) for simplicity]. A second anamorphic lens system (also not shown) is used to collect the light emerging from each row of the T_{ij} mask on individual photosites of the PD array. A bipolar T_{ij} matrix is realized in incoherent light by dividing each row of the T_{ij} matrix into two subrows, one for positive and one for negative values and bringing the light emerging from each subrow to focus on two adjacent photosites of the PD array that are electrically connected in opposition as depicted in Fig. 3(b). In the system shown in Fig. 3(a), feedback is achieved by electronic wiring. It is possible and preferable to dispose of electronic wiring altogether and replace it by optical feedback. This can be achieved by combining the PD and LED arrays in a single compact hybrid or

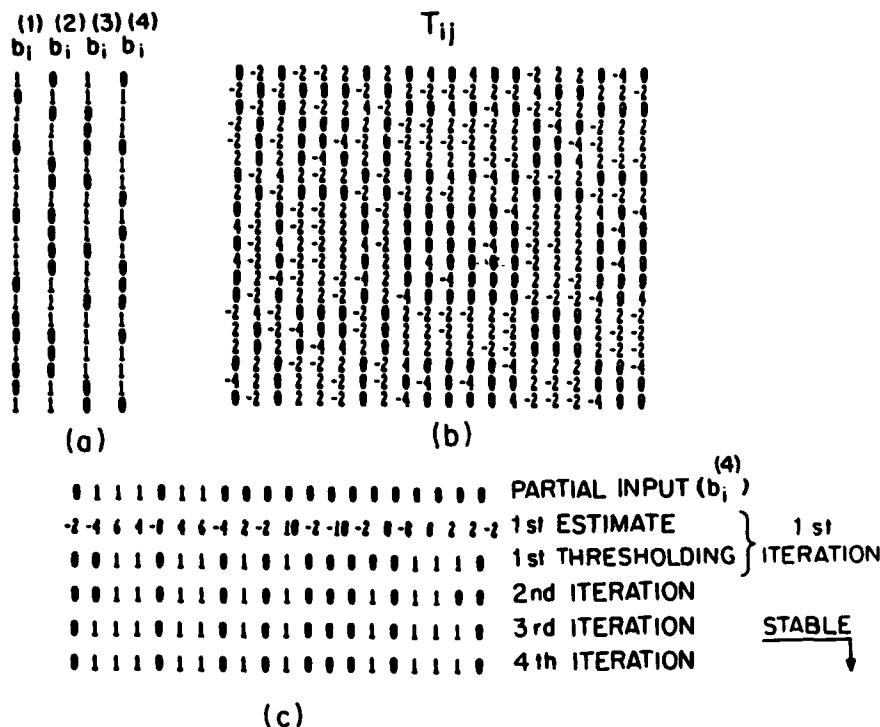


Fig. 2. Numerical example of recovery from partial input; $N = 20$, $M = 4$. (a) Stored vectors, (b) memory or (synaptic) matrix, (c) results of initializing with a partial version of $b_i^{(4)}$.

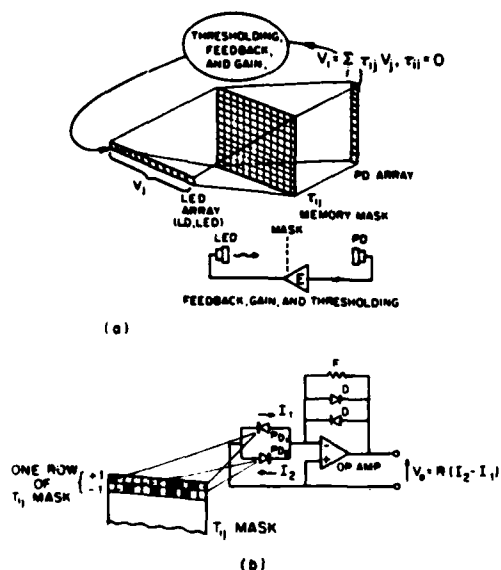


Fig. 3. Concept for optical implementation of a content addressable memory based on the Hopfield model. (a) Matrix-vector multiplier incorporating nonlinear electronic feedback. (b) Scheme for realizing a binary bipolar memory mask transmittance in incoherent light.

monolithic structure that can also be made to contain all ICs for thresholding, amplification, and driving of LEDs. Optical feedback becomes even more attractive when we consider that arrays of nonlinear optical light amplifiers with internal feedback⁹ or optical bistability

devices (OBDs)¹⁰ can be used to replace the PD/LED arrays. This can lead to simple compact CAM structures that may be interconnected to perform higher-order computations than the nearest-neighbor search performed by a single CAM.

We have assembled a simple optical system that is a variation of the scheme presented in Fig. 3(a) to simulate a network of $N = 32$ neurons. The system, details of which are given in Figs. 5–8, was constructed with an array of thirty-two LEDs and two multichannel silicon PD arrays, each consisting of thirty-two elements. Twice as many PD elements as LEDs are needed in order to implement a bipolar memory mask transmittance in incoherent light in accordance with the scheme of Fig. 3(b). A bipolar binary T_{ij} mask was prepared for $M = 3$ binary state vectors. The three vectors or words chosen, their Hamming distances from each other, and the resulting T_{ij} memory matrix are shown in Fig. 4. The mean Hamming distance between the three vectors is 16. A binary photographic transparency of 32×64 square pixels was computer generated from the T_{ij} matrix by assigning the positive values in any given row of T_{ij} to transparent pixels in one subrow of the mask and the negative values to transparent pixels in the adjacent subrow. To insure that the image of the input LED array is uniformly smeared over the memory mask it was found convenient to split the mask in two halves, as shown in Fig. 5, and to use the resulting submasks in two identical optical arms as shown in Fig. 6. The size of the subrows of the memory submasks was made exactly equal to the element size of the PD arrays in the vertical direction which were placed in register

Word 1 : 1 1 1 0 0 0 0 1 0 1 0 1 1 1 0 1 1 1 0 1 1 1 0 1 1 0 0 0 0 1 0
Word 2 : 0 1 1 0 0 0 0 0 0 0 1 0 0 1 0 1 0 0 1 1 1 1 0 1 0 1 1 0 1 0
Word 3 : 1 0 1 1 0 0 1 1 1 1 1 1 1 1 0 0 0 1 0 1 1 0 0 0 0 1 1 0 0 0

WORD	1	2	3
1	0	15	14
2	15	0	19
3	14	19	0

[illegible]

against the masks. Light emerging from each subrow of a memory submask was collected (spatially integrated) by one of the vertically oriented elements of the multichannel PD array. In this fashion the anamorphic optics required in the output part of Fig. 3(a) are disposed of, resulting in a more simple and compact system. Pictorial views of the input LED array and the

III-4

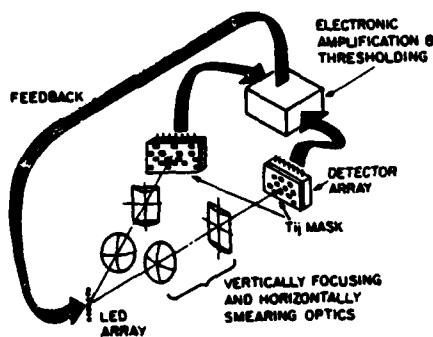


Fig. 6. Arrangement for optical implementation of the Hopfield model: (a) optoelectronic circuit diagram, (b) pictorial view.



Fig. 7. Views of (a) input LED array and (b) memory submask/PD array assemblies.

display the binary input word or vector that appears on the input LED array of the system shown in Fig. 7(a). Once an input vector is selected it appears displayed on the composing box and on the input LED box simultaneously. A single switch is then thrown to release the system into operation with the composed vector as the

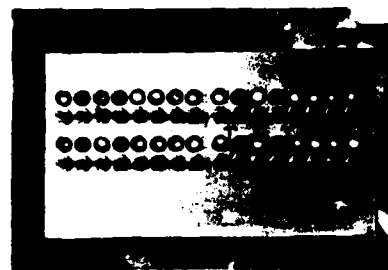


Fig. 8. Word composer and display box.

initializing vector. The final state of the system, the output, appears after a few iterations displayed on the input LED array and the display box simultaneously. The above procedure provides for convenient exercising of the system in order to study its response vs stimulus behavior. An input vector is composed and its Hamming distance from each of the nominal state vectors stored in the memory is noted. The vector is then used to initialize the CAM as described above and the output vector representing the final state of the CAM appearing, almost immediately, on the display box is noted. The response time of the electronic feedback channels as determined by the 3-dB roll-off of the amplifiers was ~60 msec. Speed of operation was not an issue in this study, and thus low response time was chosen to facilitate the experiment.

IV. Results

The results of exercising and evaluating the performance of the system we described in the preceding section are tabulated in Table I. The first run of initializing vectors used in exercising the system were error laden versions of the first word $b_i^{(1)}$. These were obtained from $b_i^{(1)}$ by successively altering (switching) the states of 1, 2, 3 . . . up to N of its digits starting from the N th digit. In doing so the Hamming distance between the initializing vector and $b_i^{(1)}$ is increased linearly in unit steps as shown in the first column of Table I whereas, on the average, the Hamming distance between all these initializing vectors and the other two state vectors remained approximately the same, about $N/2 = 16$. The final states of the memory, i.e., the steady-state vectors displayed at the output of the system (the composing and display box) when the memory is prompted by the initializing vectors, are listed in column 2 of Table I. When the Hamming distance of the initializing vector from $b_i^{(1)}$ is < 11 , the input is always recognized correctly as $b_i^{(1)}$. The CAM is able therefore to recognize the input vector as $b_i^{(1)}$ even when up to 11 of its digits (37.5%) are wrong. This performance is identical to the results obtained with a digital simulation shown in parenthesis in column 2 for comparison. When the Hamming distance is increased further to values lying between 12 and 22, the CAM is confused and identifies erroneously other state vectors, mostly $b_i^{(3)}$, as the input. In this range, the Hamming distance of the initializing vectors from any of the stored vectors is approximately equal making it more difficult for the CAM to decide. Note that the performance of

Table I. Optical CAM Performance

Hamming distance of initializing vector from $b_i^{(m)}$	Recognized vector ($m = 1$)	Recognized vector ($m = 2$)	Recognized vector ($m = 3$)
0	1 (1)	2 (2)	3 (3)
1	1 (1)	2 (2)	3 (3)
2	1 (1)	2 (2)	3 (3)
3	1 (1)	2 (2)	3 (3)
4	1 (1)	2 (2)	3 (3)
5	1 (1)	2 (2)	3 (3)
6	1 (1)	2 (2)	3 (3)
7	1 (1)	2 (2)	3 (3)
8	1 (1)	2 (2)	3 (3)
9	1 (1)	2 (2)	3 (3)
10	1 (1)	1 (1)	3 (3)
11	1 (1)	2 (2)	3 (3)
12	3 (3)	3,2 (3)	3 (3)
13	3 (3)	3 (3)	3 (2)
14	3 (3)	1,3 (1)	3 (2)
15	1 (OSC)	1 (1)	2,3 (2)
16	3 (OSC)	1 (1)	2 (2)
17	3 (OSC)	1 (OSC)	2 (2)
18	3 (3)	1 (2)	3 (OSC)
19	3 (2)	2 (2)	2 (2)
20	3 (1)	2 (2)	2 (OSC)
21	1,2 (1)	2 (2)	3 (OSC)
22	3 (1)	2 (2)	3 (OSC)
23	1 (1)	2 (2)	3 (OSC)
24	1 (1)	2 (2)	3 (3)
25	1 (1)	2 (2)	3 (3)
26	1 (1)	2 (2)	3 (3)
27	1 (1)	2 (2)	3 (3)
28	1 (1)	2 (2)	3 (3)
29	1 (1)	2 (2)	3 (3)
30	1 (1)	2 (2)	3 (3)
31	1 (1)	2 (2)	3 (3)
32	1 (1)	2 (2)	3 (3)

the CAM and results of digital simulation in this range of Hamming distance are comparable except for the appearance of oscillations (designated by OSC) in the digital simulation when the outcome oscillated between several vectors that were not the nominal state vectors of the CAM. Beyond a Hamming distance of 22 both the optical system and the digital simulation identified the initializing vectors as the complementary $b_i^{(1)}$ of $b_i^{(1)}$. This is expected because it can be shown using Eq. (1) that the T_{ij} matrix formed from a set of vectors $b_i^{(m)}$ is identical to that formed by the complementary set $b_i^{(m)}$. The complementary vector can be viewed as a contrast reversed version of the original vector in which zeros and ones are interchanged. Recognition of a complementary state vector by the CAM is analogous to our recognizing a photographic image from the negative.

Similar results of initializing the CAM with error laden versions of $b_i^{(2)}$ and $b_i^{(3)}$ were also obtained. These are presented in columns 2 and 3 of Table I. Here again we see when the Hamming distance of the initializing vector from $b_i^{(3)}$, for example, ranged between 1 and 14, the CAM recognized the input correctly as $b_i^{(3)}$ as shown in column 3 of the table and as such it did slightly better than the results of digital simulation. Oscillatory behavior is also observed here in the digital simulation when the range of Hamming distance between the ini-

tializing vector from all stored vectors approached the mean Hamming distance between the stored vectors. Beyond this range the memory recognizes the input as the complementary of $b_i^{(3)}$.

In studying the results presented in Table I several observations can be made: The optically implemented CAM is working as accurately as the digital simulations and perhaps better if we consider the absence of oscillations. These are believed to be suppressed in the system because of the nonsharp thresholding performed by the smoothly varying nonlinear transfer function of electronic circuits compared with the sharp thresholding in digital computations. The smooth nonlinear transfer function and the finite time constant of the optical system provide a relaxation mechanism that substitutes for the role of asynchronous switching required by the Hopfield model. Generally the system was able to conduct successful nearest-neighbor search when the inputs to the system are versions of the nominal state vectors containing up to ~30% error in their digits. It is worth noting that this performance is achieved in a system built from off-the-shelf electronic and optical components and with relatively little effort in optimizing and fine tuning the system for improved accuracy, thereby confirming the fact that accurate global computation can be performed with relatively inaccurate individual components.

V. Discussion

The number M of state vectors of length N that can be stored at any time in the interconnection matrix T_{ij} is limited to a fraction of N . An estimate of $M \approx 0.1N$ is indicated in simulations involving a hundred neurons or less¹ and a theoretical estimate of $M \approx N/4 \ln N$ has recently been obtained.² It is worthwhile to consider the number of bits that can be stored per interconnection or per neuron. The number of pixels required to form the interconnection matrix is N^2 . Since such a T_{ij} memory matrix can store up to $M \approx N/4 \ln N$ (N -tuples), the number of bits stored is $MN = N^2/4 \ln N$. The number of bits stored per memory matrix element or interconnection is $MN/N^2 = (4 \ln N)^{-1}$, while the number of bits stored per neuron is $MN/N = M$.

The number of stored memories that can be searched for a given initializing input can be increased by using a dynamic memory mask that is rapidly addressed with different T_{ij} matrices each corresponding to different sets of M vectors. The advantage of programmable SLMs for realizing this goal are evident. For example, the Litton Lightmod (magneto-optic light modulator), which has nonvolatile storage capability and can provide high frame rates, could be used. A frame rate of 60 Hz is presently specified for commercially available units of 128×128 pixels which are serially addressed.⁷ Units with 256×256 pixels are also likely to be available in the near future with the same frame rate capability. Assuming a memory mask is realized with a Litton Lightmod of 256×256 pixels we have $N = 256$, $M \approx 0.1N \approx 26$ and a total of $26 \times 60 = 1560$ vectors can be searched or compared per second against an initializing input vector. Speeding up the frame rate of the Litton

Lightmod to increase memory throughput beyond the above value by implementing parallel addressing schemes is also possible. Calculations show that the maximum frame rate possible for the device operating in reflection mode with its drive lines heat sunk is 10 kHz.⁷ This means the memory throughput estimated above can be increased to search 2.6×10^5 vectors/sec, each being 256 bits long, or a total of 6.7×10^8 bits/sec. This is certainly a respectable figure, specially when we consider the error correcting capability and the associative addressing mode of the Hopfield model; i.e., useful computation is performed in addition to memory addressing.

The findings presented here show that the Hopfield model for neural networks and other similar models for content addressable and associative memory fit well the attributes of optics, namely, parallel processing and massive interconnection capabilities. These capabilities allow optical implementation of large neural networks based on the model. The availability of nonlinear or bistable optical light amplifiers with internal feedback, optical bistability devices, and nonvolatile high speed spatial light modulators could greatly simplify the construction of optical CAMs and result in compact modules that can be readily interconnected to perform more general computation than nearest-neighbor search. Such systems can find use in future generation computers, artificial intelligence, and machine vision.

The work described in this paper was performed while one of the authors, N.F., was on scholarly leave at the California Institute of Technology. This author wishes to express his appreciation to CIT and the University of Pennsylvania for facilitating his sabbatical leave. The work was supported in part by the Army Research Office and in part by the Air Force Office of Scientific Research.

The subject matter of this paper is based on a paper presented at the OSA Annual Meeting, San Diego, Oct. 1984.

References

1. J. J. Hopfield, "Neural Networks and Physical Systems with Emergent Collective Computational Abilities," *Proc. Natl. Acad. Sci. USA* **79**, 2554 (1982).
2. R. J. McEliece, E. C. Posner, and S. Venkatesh, California Institute of Technology, Electrical Engineering Department; private communication.
3. G. E. Hinton and J. A. Anderson, *Parallel Models of Associative Memory* (LEA Publishers, Hillsdale, N.J., 1981).
4. T. Kohonen, *Content Addressable Memories* (Springer, New York, 1980).
5. D. Psaltis and N. Farhat, "A New Approach to Optical Information Processing Based On the Hopfield Model," in *Technical Digest, ICO-13 Conference, Sapporo* (1984), p. 24.
6. D. Psaltis and N. Farhat, "Optical Information Processing Based on an Associative-Memory Model of Neural Nets with Thresholding and Feedback," *Opt. Lett.* **10**, 98 (1985).
7. W. Ross, D. Psaltis, and R. Anderson, "Two-Dimensional Magneto-Optic Spatial Light Modulator For Signal Processing," *Opt. Eng.* **22**, 485 (1983).
8. J. W. Goodman, A. R. Dias, and L. M. Woody, "Fully Parallel, High-Speed Incoherent Optical Method for Performing Discrete Fourier Transforms," *Opt. Lett.* **2**, 1 (1978).
9. Z. Porada, "Thin Film Light Amplifier with Optical Feedback," *Thin Solid Films* **109**, 213 (1983).
10. H. M. Gibbs *et al.*, "Optical Bistable Devices: The Basic Components of All-Optical Circuits," *Proc. Soc. Photo-Opt. Instrum. Eng.* **269**, 75 (1981).

END

12-86

DTIC